Surveys in Geophysics
https://doi.org/10.1007/s10712-025-09909-4

Using Atmospheric Waves for the Detection and Early Warning of Natural Hazards: A Review Combining Results from the Neutral Atmosphere and the Ionosphere

Sabine Wüst[1] · **Marco Guerra**[2,3] · **Jaroslav Chum**[4] · **L. Claire Gasque**[5]

Received: 28 March 2025 / Accepted: 18 September 2025

Abstract
Waves transport energy through the atmosphere without transporting mass. Often excited in the troposphere, they can propagate horizontally and vertically over long distances, depending on the type of wave and the background atmosphere. The fastest atmospheric waves are (infra)sound and acoustic gravity waves. The list of possible reasons for the generation of these atmospheric waves is not short; here, we concentrate on natural hazards. Due to their comparatively high propagation speed, infrasound and acoustic gravity waves can contribute to or even improve early warning of natural hazards, even when measured at high altitudes. Traditionally, each scientific community—the one that deals with the neutral atmosphere and the one that addresses the ionosphere—usually works on its own. The aim of this manuscript is to bring together observations and results from both communities. The main challenges of the respective communities with regard to the use of these waves in the context of early warning of natural hazards are identified.

Keywords Upper mesosphere/lower thermosphere · Ionosphere · Natural hazards · Acoustic gravity waves · Infrasound · Travelling ionospheric disturbances

1 Introduction

Waves transport energy through the atmosphere without transporting mass (e.g., Nappo (2012)). Often generated close to the ground, they can propagate horizontally and vertically over long distances, affecting not only the neutral atmosphere, but also the ionized parts of the atmosphere, the ionosphere. The distance they travel depends on the type of the wave (planetary or gravity or infrasound waves) and the background atmosphere. Waves transport and redistribute energy in the atmosphere (e.g., Rauthe et al. (2008), Ern et al. (2011), Kramer et al. (2015), Wüst et al. (2016, 2017a, 2025)) and are therefore an important factor in understanding and modelling the behaviour of the atmosphere (e.g., Alexander et al. (2010), Geller et al. (2013)). Prominent sources for atmospheric waves influencing the neutral atmosphere and ionosphere are associated with natural hazards including earthquakes, tsunamis, and volcanic eruptions (e.g., Benioff et al. (1951), Hines (1972), Kanamori et al. (1994)). The eruption of the Hunga Tonga–Hunga Ha'apai in 2022, which

---

Extended author information available on the last page of the article generated atmospheric waves that circled the globe multiple times, is perhaps the most notable recent example (e.g., Wright et al. (2022)). Fast waves in particular can contribute to early warning of natural hazards, if their signals can be measured in near real time and correctly attributed to a natural hazard. This is especially useful for regions of the Earth that are less well equipped with other early warning mechanisms, and for natural hazards that are difficult to measure early and that could benefit from additional information, such as tsunamis.

This manuscript reviews the potential of atmospheric wave measurements at altitudes above 80 km to be used for early warning of natural hazards. However, it does not cover observations or mechanisms related to potential precursors of these hazards. Readers interested in that topic are referred to Nemec et al. (2008), Harrison et al. (2010), Liu et al. (2010), Pulinets and Davidenko (2014), Kuo et al. (2014), and Liu et al. (2024), for example.

In recent years, various review papers have been published on the use of primarily ionospheric measurements for the observation, modelling and early warning of natural hazards. This often involves not only the detection of ionospheric disturbances but also of ground movements. Bock and Melgar (2016), for example, address the relevant concepts of geodetic theory, data analysis and physical modelling of a variety of processes that influence the GNSS signal. Amongst them are also atmospheric disturbances from natural hazards. They discuss the integration of further data sets from geodesy, seismology, and geology. Komjathy et al. (2016) specialize in ground-based and space-borne measurements of the total electron content (TEC) of the ionosphere, the latter derived from GNSS measurements. They put emphasis on the modelling of TEC disturbances caused by natural hazards and also report advancements in estimating tsunami wave heights and ground surface displacements. Astafyeva (2019) and Hohensinn et al. (2024) focus on ionospheric monitoring of different natural hazards (earthquakes, tsunamis, and volcanic eruptions, in the case of Astafyeva (2019) and earthquakes, landslides, volcanoes, and tropospheric hazards (severe weather) in the case of Hohensinn et al. (2024)). They focus on GNSS measurements and TEC information derived from them. Both bring up further perspectives: Hohensinn et al. (2024)), for example, discusses the advantages and disadvantages of GNSS measurements and how they can be integrated with other sensors such as seismometers or radar (Interferometric Synthetic Aperture Radar, InSAR); Astafyeva (2019) puts more focus on the future development of ionosphere-based methods and modelling. To the best of the authors' knowledge, Meng et al. (2019) is the only review article that puts at least some emphasis to measurements of the neutral atmosphere. The article addresses impulsive surface disturbance events (e.g. earthquakes, tsunamis, volcanic eruptions and explosions) as a source of acoustic-gravity waves, which can be detected using radar, GNSS, ground-based radio occultation and airglow measurements. However, they focus on the red oxygen airglow, which forms a comparatively broad layer peaking around 250 km (e.g. Haider et al. (2022)), rather than the comparatively narrow hydroxyl airglow layer around 86 km height (Wüst et al. 2020). Mesospheric airglow is considered in terms of satellite-based measurements (TIMED-SABER, Thermosphere Ionosphere Mesosphere Energetics Dynamics, Sounding of the Atmosphere using Broadband Emission Radiometry), a limb-looking instrument.

In this article, measurements of the neutral and the ionized atmosphere are addressed. However, in comparison with Meng et al. (2019), there is much more focus on neutral atmosphere measurements, especially on ground-based ones of the hydroxyl airglow. This airglow layer has a comparatively small thickness, which allows the detection of much shorter vertical wavelengths than ground-based measurements of the red oxygen airglow do. Furthermore, it has a lower centroid height than the red oxygen airglow; this favours an earlier detection of atmospheric waves generated at lower altitudes. Finally, ground-based hydroxyl airglow measurements are made at various locations around the world (see e.g. the Network for the Detection of Mesospheric Change, NDMC, https:\ \ndmc.dlr.de). The first measurements date back to the 1950s. The manuscript is structured as follows: The emphasis in Sect. 2 is on a solid presentation of the basic theoretical principles of atmospheric waves and their propagation through the neutral and ionized atmosphere. In addition, different types of atmospheric waves are considered. Section 3 reviews the neutral atmospheric and ionospheric signatures of natural hazards and how they have been historically measured and modelled. Section 4 summarizes the status of challenges associated with an atmospheric natural hazard early warning system. The manuscript ends with Sect. 5, a summary and conclusion.

2 Vertical Coupling Through Waves

The atmosphere can sustain a variety of waves, which arise when its equilibrium state is perturbed and a restoring force acts to bring it back to equilibrium. One of the most common distinctions between waves in atmospheric physics is based on which forces in the wave dispersion relation (from the set of pressure gradient force, gravitational force, and Coriolis force) are dominant or negligible. All three forces are initially taken into account in the Navier–Stokes equation, which describes the forces acting on an air parcel. In addition, the conservation of energy is assumed and the first law of thermodynamics is applied. Transforming these equations and applying some approximations as shown, for example, by Pichler (1997) or Gossard and Hooke (1975) leads to a system of equations that can be solved using a plane wave approach. The following dispersion relation, which is valid for all atmospheric waves, can then be derived:

$$m^2 = \frac{\left(N^2 - \hat{\omega}^2\right){k_h}^2}{\hat{\omega}^2 - f^2} + \frac{\hat{\omega}^2}{c_s^2} - \left(\frac{N^2}{{c_s}^2} + E^2\right) \tag{1}$$

with the wave vector (k, l, m) and the vector of its horizontal part $\mathbf{k}_h = (k, l)$, N the Brunt-Väisälä frequency, c_s the sound speed, $\hat{\omega}$ the intrinsic frequency, so the frequency that is observed by someone who is moving with the background wind, f the Coriolis frequency, and E the Eckhart coefficient. The Eckhart coefficient is often neglected, e.g. in the Boussinesq approximation. The same holds for $\frac{N^2}{{c_s}^2}$, which is of a similar order of magnitude (10^{-9}–10^{-8}, as N varies typically around $2{\cdot}10^{-2}$ 1/s and c_s around $3{\cdot}10^2$ m/s). However, sometimes the Eckhart coefficient is also approximated by $\frac{1}{2H}$ in an isothermal atmosphere. Doing this, Eq. (1) becomes

$$m^2 = \frac{\left(N^2 - \hat{\omega}^2\right){k_h}^2}{\hat{\omega}^2 - f^2} + \frac{\hat{\omega}^2}{c_s^2} - \frac{1}{4H^2} \tag{2}$$

For the purpose of application in the field of early warning of natural hazards, the focus should be on comparatively fast waves: terms including the speed of sound in Eq. (2) should therefore not be neglected. This means that the medium is compressible and c_s does not go to infinity. However, large scale waves (for which the Coriolis frequency plays a role) can be omitted. This is done by setting f equal to zero. Also pure gravity waves can

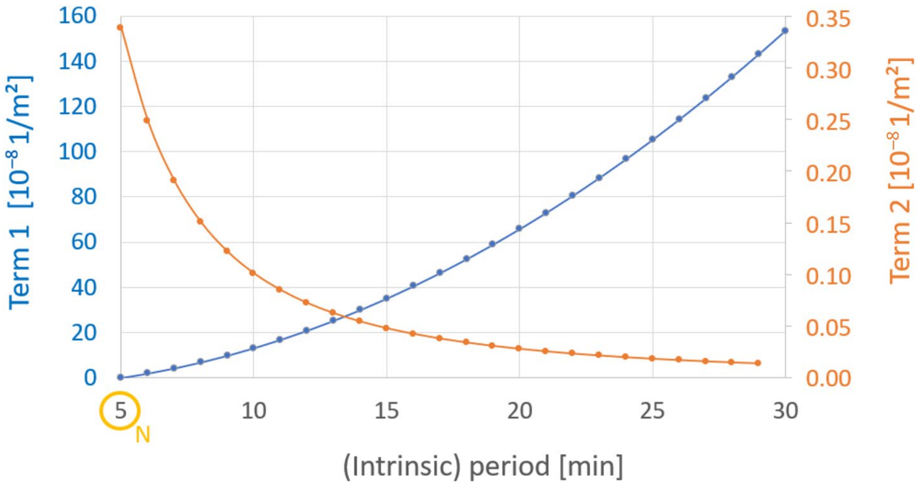

Fig. 1 Term 1 in Eq. (3) that is $\frac{(N^2-\hat{\omega}^2){k_h}^2}{\hat{\omega}^2}$ and term 2 that is $\frac{\hat{\omega}^2}{c_s^2}$ behave differently for increasing intrinsic periods. Please be aware of the different orders of magnitude on the y-axes. For this figure, the Brunt-Väisälä period is assumed to be five minutes (marked in yellow on the x-axis), the sound speed is 300 m/s, background winds are neglected and the horizontal wavelength is set to 30 km. For an intrinsic period equal to the Brunt-Väisälä period, term 1 is zero, while term 2 is larger than zero. For an intrinsic period of 10 min, term 1 is already an order of magnitude greater than term 2

be excluded, as their phase speed is much smaller than the sound speed (their dispersion relation would follow from Eq. (2) by assuming c_s approaches infinity). Acoustic gravity waves, however, are to some extent a hybrid between gravity waves and acoustic waves: they have an intrinsic frequency somewhat smaller than but comparable to the Brunt-Väisälä frequency (Yeh and Liu 1974); the compressibility of the atmosphere and therefore the speed of sound cannot be set to infinity. Their dispersion relation is

$$m^2 = \frac{\left(N^2 - \hat{\omega}^2\right){k_h}^2}{\hat{\omega}^2} + \frac{\hat{\omega}^2}{c_s^2} - \frac{1}{4H^2} \tag{3}$$

As gravity acts only in the vertical direction, the related wave process is highly anisotropic. Only for intrinsic frequencies very near to the Brunt-Väisälä frequency the first term in Eq. (3), $\frac{(N^2-\hat{\omega}^2){k_h}^2}{\hat{\omega}^2}$, is less than the second term, $\frac{\hat{\omega}^2}{c_s^2}$ (see Fig. 1) and it becomes zero when $\hat{\omega}$ approaches N. Otherwise, the first term dominates: the smaller the intrinsic frequency (the larger the intrinsic period), the larger the first term and the smaller the second term becomes. This growth of the first term with decreasing intrinsic frequency (increasing intrinsic period) leads to (intrinsic) vertical phase speeds $c_z = \frac{\hat{\omega}}{m}$ being too slow in the context of early warning (see Fig. 2).

The dispersion relation for pure sound waves is derived from Eq. (3) by neglecting gravity ($N = 0$) and the stratification of the atmosphere ($E^2 \approx \frac{1}{4H^2} = 0$):

$$m^2 = -{k_h}^2 + \frac{\hat{\omega}^2}{c_s^2} \tag{4}$$

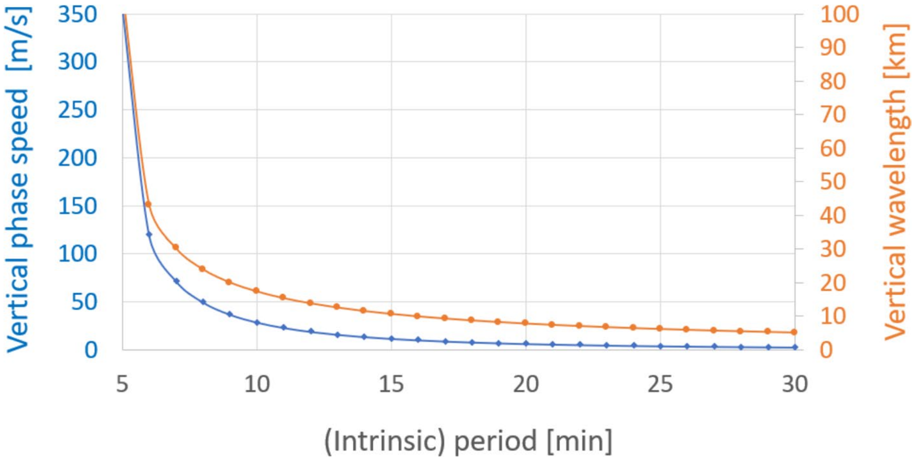

Fig. 2 The vertical wavelength and phase speed decrease with increasing intrinsic period. The assumptions are the same as for Fig. 1. Additionally, the scale height is assumed to be 13 km (according to CIRA for a height of ca. 90 km). In this example, waves with an intrinsic period equal to $\frac{2\pi}{N}$ reach 90 km height after ca. 5 min, waves with an intrinsic period equal to 30 min need more than 8 h

$$\Leftrightarrow \frac{\hat{\omega}^2}{k^2 + l^2 + m^2} = c_s^2 \tag{5}$$

This shows that in contrast to gravity waves and acoustic gravity waves, sound waves are not dispersive; their speed of propagation c_s is $\sqrt{\frac{c_p}{c_V}RT}$ with c_p and c_V the specific heat capacity for constant pressure p or volume V and R the specific gas constant. Their intrinsic frequency is much higher than the Brunt-Väisälä frequency (indeed they can approach the acoustic cut-off frequency $\frac{c_s}{2H}$ which is larger than the Brunt-Väisälä frequency) and gravity effects play no role.

From the dispersion relations (3) and (4), it becomes clear that the speed of propagation of acoustic waves is higher than that of acoustic gravity waves. While sound waves have phase speeds of around 300 m/s up to 100 km height and can reach up to 1,000 m/s above (Lognonné et al. (2006) and see Fig. 3c), the vertical phase velocity of acoustic gravity waves, which are dispersive, is always less (see Fig. 1 and Eq. (3) and neglect the approximation of the Eckhart coefficient). This means acoustic waves reach the upper mesosphere and lower thermosphere, UMLT, and therefore the lower part of the ionosphere ca. 5–10 min after their generation (see Fig. 3c and 4c). For acoustic-gravity waves, it takes longer.

In addition to gravity waves, acoustic gravity waves and acoustic waves, there are also some special cases of waves that are mentioned in connection with natural hazards. These include lamb waves and shock waves. Like sound waves, shock waves and Lamb waves are longitudinal waves. The latter propagate purely horizontally at the speed of sound, with the air particles oscillating horizontally. Their vertical wave number is imaginary, so their propagation is attenuated in the vertical direction. Accordingly, their pressure amplitude is highest at the ground (Gossard and Hooke (1975)). A shock wave is created when the generating body moves with constant acceleration through a comparatively stationary medium. The generating body causes the gas to compress and thus the temperature to rise. This also

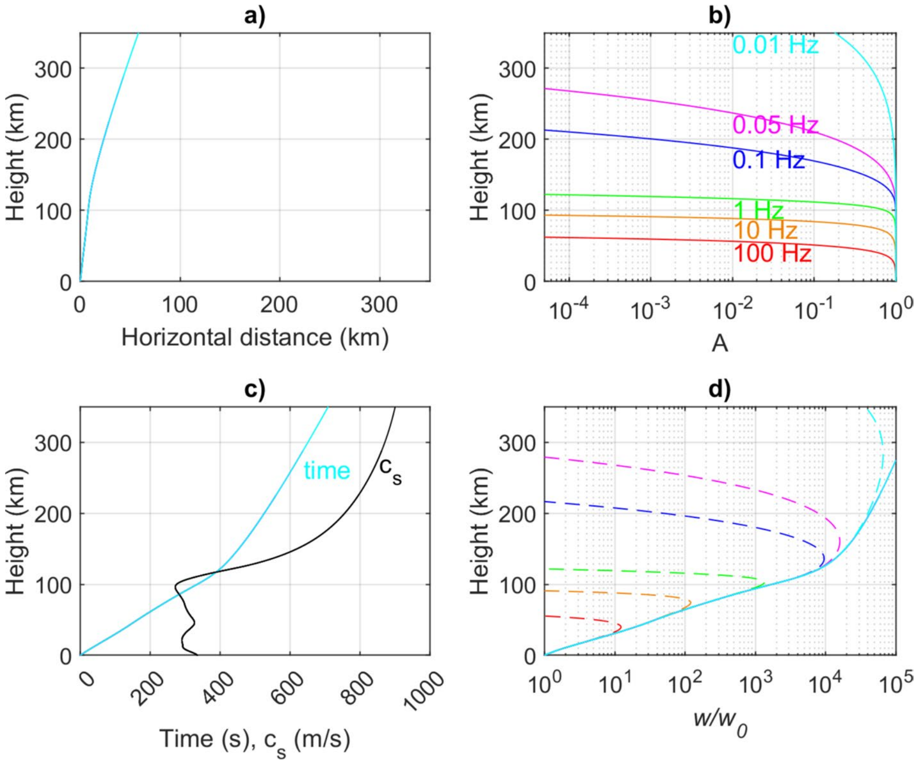

Fig. 3 Ray tracing results for the infrasound waves started from the surface with zenith angle 5°. **a** Ray trajectories in vertical cross section. **b** Attenuation A as a function of height (relative to initial value) calculated by the analytic model assuming a wave frequency of 0.01, 0.05, 0.1, 1, 10 and 100 Hz and based on the formulas presented by Bass et al. (1984) and Chum et al. (2012) **c** Propagation time and sound speed c_S as a function of height. **d** Ratio of air particle oscillation velocities w at a specific height related to the near surface value w_0. The solid line represents the unrealistic lossless propagation for which the quantity $c_S \rho w^2$ is conserved, where ρ is the background air density

increases the speed of the waves (and thus the local speed of sound), and waves generated later catch up with those generated earlier. Eventually, a thin shock front is formed within which one or more physical properties, such as velocity, change abruptly (Billingham and King (2000)).

The ionized atmosphere, the ionosphere, is often described as the area between ca. 60 and 800 km altitude, with the D-layer at 60–90 km, the E-layer at 90–120 km and the F-layer at 120–800 km. The maximum ionized density (referred to as the peak of the F2-layer) usually lies between 250 and 400 km altitude. When atmospheric waves generated in the neutral atmosphere reach ionospheric altitudes, they can couple to and modulate ionospheric plasma. Plasma-neutral coupling between the ionosphere and neutral atmosphere is complicated by the fact that, in the ionosphere, electrons and ions are subject to electromagnetic forces in addition to the forces governing the neutral atmosphere.

The ease with which charged particles can move through the ionosphere is described by the ionospheric conductivity, which varies with altitude and is highly anisotropic with respect to the direction of Earth's magnetic field. The *parallel conductivity*, $\sigma_{\|}$, affects magnetic field-aligned currents. The *Pedersen conductivity*, σ_P, affects currents in the direction

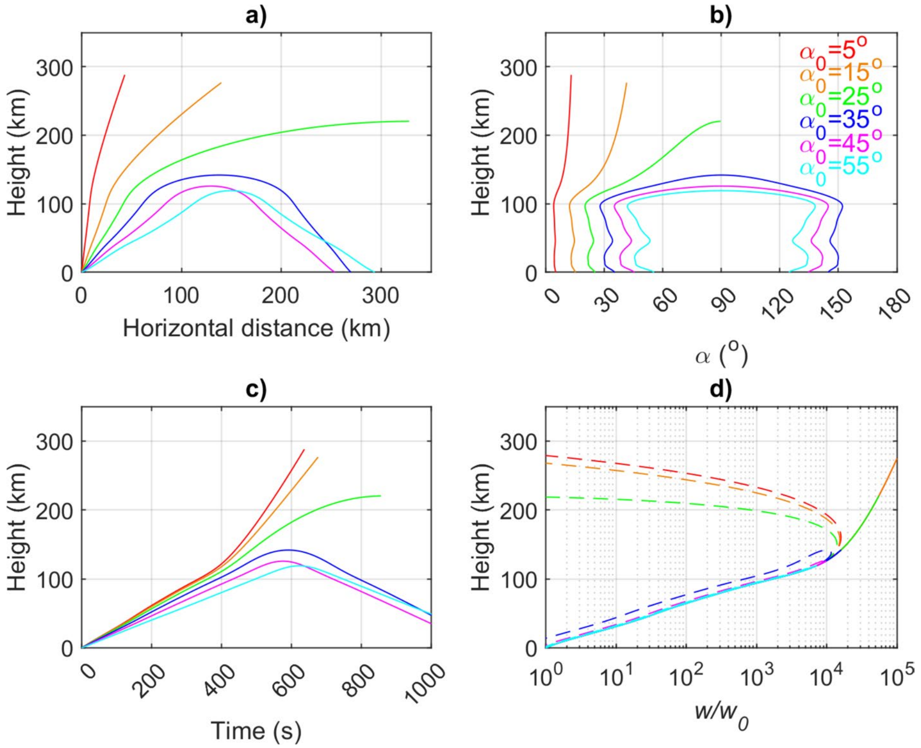

Fig. 4 Ray tracing results for the infrasound waves of frequency 0.05 Hz started with zenith angles 5°, 15°, 25°, 35°, 45° and 55°. **a**Ray trajectories in vertical cross section. **b** Evolution of the zenith angle α with height **c** Propagation time as a function of height. **d** Ratio of air particle oscillation velocities w at a specific height related to the near surface value w_0. Solid line represents the unrealistic lossless propagation for which the quantity $c_S \rho w^2$ is conserved, where ρ is the background air density

of the component of the electric field which is perpendicular to the magnetic field ($\vec{E}_\perp$). The *Hall conductivity*, σ_H, affects currents perpendicular to both the electric and magnetic field. Typical values of these conductivities in the mid-latitude ionosphere are displayed in Fig. 5a.

The large ionospheric parallel conductivity allows charges to quickly respond to magnetic field-aligned forces by flowing along the magnetic field. However, in the perpendicular direction, their behaviour is highly dependent on the electron and ion gyrofrequencies as well as the electron-neutral and ion-neutral collision frequencies, which change with altitude, as shown in Fig. 5b (inspired by figure 4.10 of Baumjohann and Treumann (2012)). Below the so-called dynamo layer, the collision frequencies are greater than the gyrofrequencies for both species, meaning that charges cannot complete one gyration around the magnetic field before colliding with a neutral particle. Here, ions and electrons move with the neutral atmosphere, regardless of the direction of the magnetic field. At the base of the dynamo layer, the electron gyrofrequency is greater than the electron-neutral collision frequency but the ion gyrofrequency is less than the ion-neutral collision frequency, meaning that electrons are magnetized and drift according to electromagnetic forces, but ions move with the neutrals. This differential electron/ion motion results in a Hall current perpendicular to the electric and magnetic

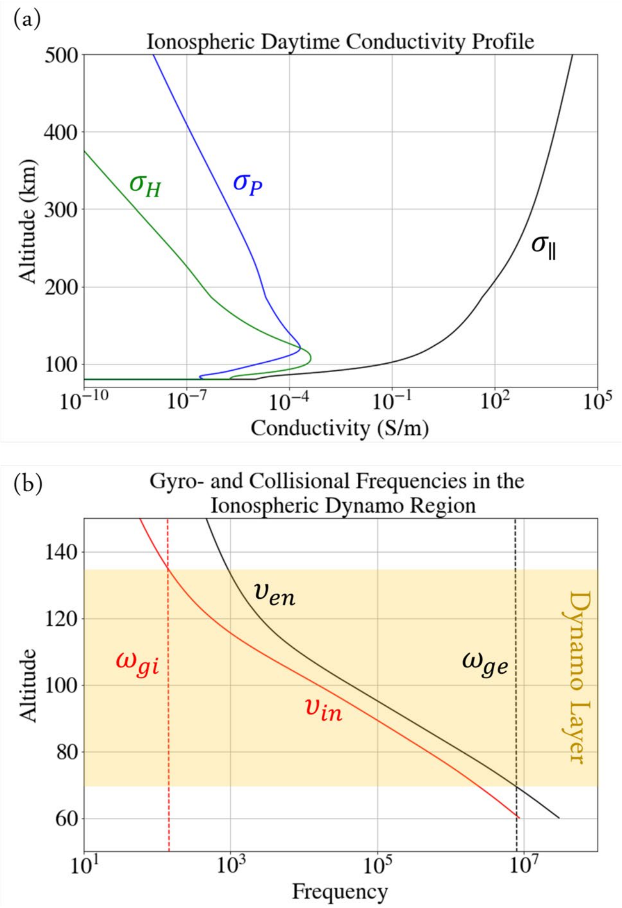

Fig. 5 **a** Typical values of the Pedersen (σ_P), Hall (σ_H) and parallel ($\sigma_\parallel$) conductivity in the mid-latitude daytime ionosphere. **b** Representative mid-latitude profiles of ionospheric gyrofrequencies (ion gyrofrequency ω_{gi}, electron gyrofrequency ω_{ge}) and plasma-neutral collisional frequencies (ion neutral frequency ν_{in}, electron neutral frequency ν_{en}), inspired by figure 4.10 of Baumjohann and Treumann (2012)

fields. Higher in the dynamo layer, where the ion-neutral collision frequency becomes comparable to the ion gyrofrequency, ions will move in the direction of the electric field and therefore carry a Pedersen current, while electrons still carry a Hall current. Above this layer, both electrons and ions are magnetized, so their motion is mainly restricted along the magnetic field. As a result, different magnetic field configurations can lead to variations in the effectiveness of coupling between neutral atmosphere and ionospheric waves (Bagiya et al. (2019), Rolland et al. (2011), Rolland et al. (2013)).

Travelling ionospheric disturbances (TIDs), which are most often measured as modulations in the ionospheric total electron content (TEC), an integrated quantity which therefore most closely traces the density of the peak of the ionospheric F-layer, can be formed through either direct plasma-neutral collisions which move plasma along field lines, or they can have their origin in the dynamo region when electric fields arise which can then map along the magnetic field to affect plasma at different altitudes and in the conjugate hemisphere. TIDs are commonly categorized according to their wavelengths and periods. Medium-scale TIDs (horizontal wavelengths of a few hundreds of kilometres and typical periods from approximately 10 to 60 min) are usually thought to be related to gravity waves associated with lower atmospheric sources (Hocke (1996)). In contrast, large-scale TIDs (horizontal wavelengths of a few thousand kilometres and typical periods from one to several hours) are primarily associated with auroral heating during periods of intense geomagnetic activity (e.g., Jonah et al. (2018), Lyons et al. (2019)). Simultaneous observations of ionospheric perturbations at magnetically conjugated points have also been reported (e.g., Huba et al. (2015), Martinis et al. (2011)).

Not all atmospheric waves that are excited in the lower part of the atmosphere also reach heights above 80 km. One of the key aspects of neutral wave propagation in the atmosphere is its strong dependence on background conditions. As such, both gravity and acoustic waves increase in amplitude with height as the atmospheric density decreases due to energy conservation (Hines (1960)). This amplification factor is estimated to be around 10^4 in the lower thermosphere (approximately 150 km) and can reach up to 10^{5-6} at peak ionospheric density heights (Blanc et al. (2009), Lognonné et al. (2006)). On the other hand, damping effects are inversely proportional to atmospheric density, meaning that wave energy dissipation becomes stronger at higher altitudes. Energy damping is more pronounced for higher frequency waves, indicating that the atmosphere acts as a low-pass filter (see Fig. 3b). For gravity waves, these effects are only important in the thermosphere. At the OH*-airglow layer height filtering by the background wind is more important. The momentum and energy of waves in the thermosphere decrease mainly due to the kinematic viscosity and thermal conductivity losses, respectively (Vadas et al. (2005)).

Figure 3a shows ray trajectories of infrasound waves originating at the ground with a zenith angle α=5°, which is a typical angle for infrasound waves generated by coherent seismic waves outside the epicentre region. The quasi-vertical orientation of infrasound waves is due to supersonic speeds c_G of the seismic waves: the infrasound waves are generated with an initial zenith angle α given by $sin(\alpha) = c_{S_0}/c_G$, where c_{S_0} is the sound speed just above the ground surface (Rolland et al. (2011); see figure 1 in Chum et al. (2016b)). In Fig. 4a the trajectories are shown for different zenith angles, which is the usual situation close to the epicentre, and a frequency of 0.05 Hz. This is a typical frequency of infrasound generated by seismic waves (e.g. Haralambous et al. (2023)). It becomes clear that the altitude of F layer is only reached by waves with initial zenith angles smaller than about 25° (green line). In addition, waves starting at higher zenith angles are more attenuated at the same height (if they reach it) due to longer propagation in a medium with high kinematic viscosity. It should also be noted that the energy flux decreases due to geometrical spreading: if the infrasound trajectories diverge, i.e. the area traversed by them becomes larger, the energy flux must become smaller due to energy conservation.

3 Atmospheric Waves in the Neutral and Ionized Atmosphere Caused by Natural Hazards

Natural hazards are known to excite different types of neutral waves (i.e., waves in the neutral atmosphere), with a specific relationship between the generating phenomenon and the associated neutral waves. Acoustic waves are typically associated with earthquakes, explosive volcanic eruptions (Astafyeva (2019)) and anthropogenic explosions (Jonah et al. (2021)). Acoustic waves generated by high-energy events, such those in the near-field of large earthquakes, can evolve into N-shaped shock waves due to nonlinear effects. (Acoustic) gravity waves are typically generated by tsunamis, volcanic eruptions, and extreme tropospheric weather events (Astafyeva (2019)). The following is an overview of measurements of such waves associated with natural hazards and their modelling. This section is divided into neutral and ionised atmosphere studies but first the underlying measurements techniques are briefly introduced.

3.1 Detection Techniques

As mentioned above, the focus of this manuscript is on measurements at 80 km height and above. We address the non-ionized, i.e. the neutral atmosphere and the ionized atmosphere. Both cannot be clearly separated, they co-exist. Up to low earth orbit (about 500 km), the neutral density is typically several orders of magnitude higher than the ion density. Therefore, waves at the same altitude can be detected by measurements of the neutral atmosphere and the ionosphere. For the following literature study, we mainly focus on the results achieved with specific techniques. We choose primarily OH* airglow measurements for the neutral atmosphere and GNSS, Doppler and ionosonde measurements for the ionized atmosphere.

OH* airglow measures the neutral atmosphere with a centroid height of ca. 85–87 km (e.g., Shepherd et al. (2006); von Savigny (2015); Wüst et al. (2017b, 2020)). In contrast to the red airglow, which is due to atomic oxygen showing a peak altitude around 250 km, the OH* airglow layer and also the other airglow layers between 90 km and 100 km are narrow (ca. 6–9 km full width at half maximum for OH*) and therefore better suited for the investigation of atmospheric waves, at least when it comes to measurement techniques that integrate vertically. The neutral atmosphere around 90 km can be investigated not only by airglow-based techniques, but also by active remote-sensing instruments such as specific radar or lidar systems. However, those techniques integrate in most cases over one hour (e.g., Rauthe et al. (2008); Wüst et al. (2018) and citations therein) to reach a sufficient signal-to-noise ratio. Using passive remote sensing of OH* airglow from the ground, information about this altitude range has been collected for about 100 years (Meinel (1950)). The technical development has made it possible to measure with a temporal resolution of less than 1 s for about 10–15 years now (e.g., Hannawald et al. (2016), Sedlak et al. (2016)). With this temporal resolution, at least parts of the infrasound range (frequencies lower than 16 Hz) can be addressed. In the case of observing OH* airglow transitions for which local thermodynamic equilibrium (LTE) holds, not only the intensity (which is defined differently by different authors and is therefore an ambiguous term) of the transition can be measured also the kinetic temperature can be estimated. The signal is always integrated vertically over the OH*-airglow layer when measured by a ground-based instrument looking into the sky. The longer the vertical wavelengths—and high-frequency gravity waves as well as mainly vertically propagating infrasound are associated with comparatively long vertical wavelengths—the less important this averaging effect becomes. An overview of OH*-airglow measurements and their use for investigating atmospheric dynamics can be found in Wüst et al. (2023).

In the ionosphere, one of the most common measurements used to detect TIDs is TEC maps derived from GNSS measurements. Since the ionospheric density typically has a distinct peak at around 200–400 km, TEC measurements are typically mapped to an altitude representative of this peak height. Moreover, due to the slant nature of GNSS measurements, a single ground-based GNSS receiver can sense points that are as far as 1,000 km from the receiver location. Other traditional instruments used to probe the ionosphere include ionosondes and Continuous Doppler Sounding Systems (CDSS). Ionosondes are used to retrieve electron density profiles from the E layer up to the peak of the plasma density (usually the peak of the F2 layer). However, several phenomena can disrupt ionosonde profile retrieval, such as spread-F (equatorial plasma bubbles) and sporadic E layers. CDSS is a system composed of a high frequency transmitter and receiver that works at a constant frequency. By continuously emitting at a constant frequency, it is possible to determine the plasma movement at the height of the reflecting layer by studying the induced Doppler frequency shift. By transmitting at various frequencies, CDSS can study different layers of the ionosphere, as there is a direct relationship between the signal frequency and the plasma density of the reflecting layer.

3.2 Neutral Atmosphere

3.2.1 Infrasound or acoustic gravity waves in OH*-airglow measurements

The idea that natural hazards such as tsunamis produce atmospheric waves and that these can propagate to heights of over 80 km was discussed and investigated as early as the 1970s (e.g., Hines (1972), Najita (1976)). However, due to technical developments, the period range of infrasound has only been accessible in OH* airglow measurements, at least partially, since approximately 15 years ago. Waves with periods close to the Brunt-Väisälä frequency, which are typical for acoustic gravity waves, have been observed for several decades. Krassovsky (1972) was probably one of the first to report the observation of fluctuations with a period of 5–10 min in OH* intensity and temperature measurements. Although that article repeatedly refers to "acoustic-gravitational waves", from today's point of view these are acoustic gravity waves, or at least high-frequency gravity waves.

One of the first statistical analyses of fluctuations with a duration of 2.5 to 10 min appeared a good 10 years ago: Pilger et al. (2013a) analysed 40 months of ground-based OH* temperature measurements at four different European sites and found more than 13,000 significant fluctuations in this period range (Figs. 7 and 8 of their publication show the corresponding histograms). Bittner et al. (2010) revisited the idea of infrasound airglow measurements and the aspect of early warning of tsunamis and other geo-hazards and showed that indications of periodic fluctuations in the infrasound range can be detected in ground-based spectrometer measurements. The authors speculated that the observed signals were due to meteorological and orographic sources. Pilger et al. (2013b) presented similar results regarding the sources, but also provided a corresponding detection algorithm based on the application of different spectral analyses. To the best of our knowledge, Le Dû et al. (2020) was the first to show a spatial signature with a period significantly smaller than the Brunt-Väisälä period and propagating at sound speed in OH* airglow imager measurements in a case study (Fig. 6). However, it is probably not due to a natural hazard.

While there are few fundamental publications on the observation of infrasound in general or acoustic gravity waves induced by natural hazards in OH* airglow, modelling is more advanced. In his publication, Snively (2013) generally addresses convective tropospheric sources, which generate acoustic waves in addition to concentric gravity waves. The author uses a numerical model to determine the characteristics of acoustic and gravity waves observable in OH* airglow (integrated intensity and brightness-weighted temperature) and generated by idealised transient tropospheric updrafts.

Inchin et al. (2020), Inchin et al. (2022), and Inchin et al. (2022) extended this modelling further, using seismic wave propagation models as lower boundary conditions for the vertical velocity of surface motions. They simulated the hypothesized but unobserved response of the OH* airglow layer to the 2016 M7.8 Kaikoura earthquake in New Zealand (Inchin et al. (2022)), the 2011 Tohoku-Oki tsunami in Japan (Inchin et al. (2020)) as well as seven further tsunamis caused by earthquakes with a magnitude between 7.7 and 9.1 (Inchin et al. (2022)).

For the Kaikoura earthquake, which is considered to belong to the most complex inland earthquakes, the strongest estimated infrasound-induced peak-to-peak perturbations reach ca. 18% relative to the background state in the vertically integrated volume emission rate of the OH(3-1) emission and ca. 5.8 K (3.2%) in the brightness weighted temperature. The infrasound exhibits periods of 30–45 s and vertical wavelengths of 7–11 km. Very valuable from an observer's point of view is Fig. 9. It depicts the synthetic observations of airglow imaging systems (differing in zenith angle, temporal resolution and observed species) showing the evolution of the earthquake-induced and ring-like infrasound structures.

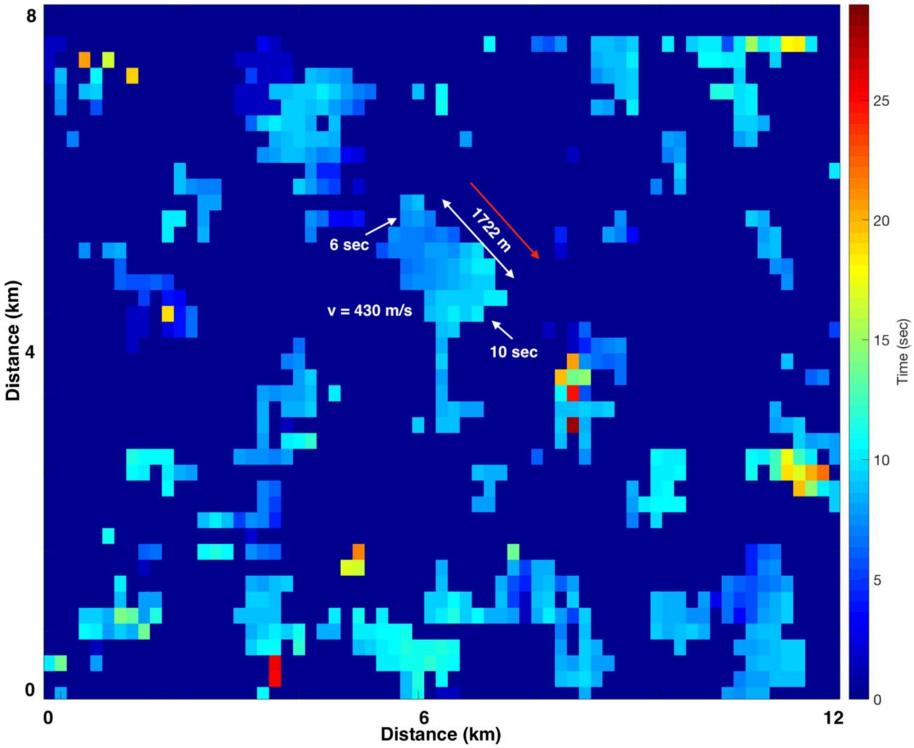

Fig. 6 Shown is the propagation of a perturbation with a period of 5 s for a part of an OH* airglow image. The colour code refers the onset time of the perturbation. The red arrow depicts the direction of propagation. The horizontal speed of propagation is 430 m/s. Reprinted under CC-BY−4.0 license from Le Dû et al. (2020) ©2020, The Author(s)

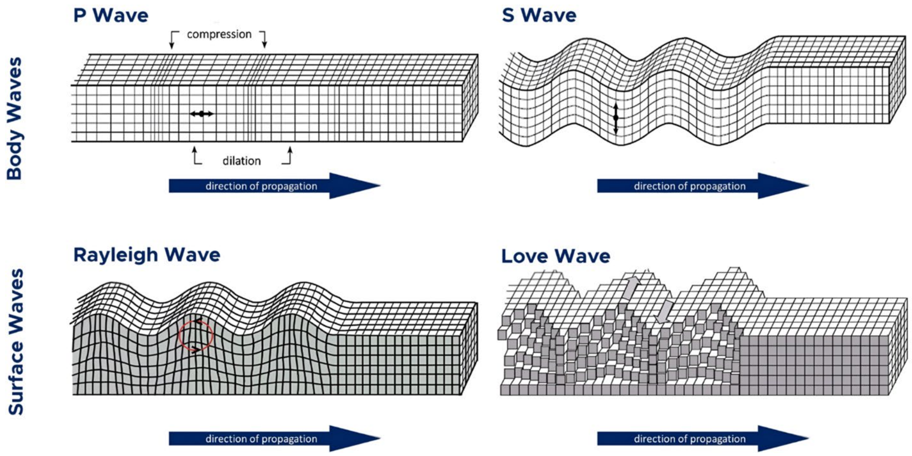

Fig. 7 While P and S waves are body waves, Rayleigh and Love waves are surface waves. P waves are longitudinal waves, S waves and Love waves are transverse ones. (LukeTriton, Steven Earle, Mario Baić, Lovorka Librić, Danijela Jurić Kaćunić https://upload.wikimedia.org/wikipedia/commons/0/07/Overview_Seismic_Waves.jpg, Meho Saa Kovaević, CC BY-SA 4.0 https://creativecommons.org/licenses/by-sa/4.0 via Wikimedia Commons)

Inchin et al. (2020) and Inchin et al. (2022) focus on seaquakes. As bottom boundary conditions of the atmospheric model ocean surface velocities are taken. While Inchin et al. (2020) make the assumption that the ocean compressibility is negligible and therefore the ocean surface height changes according to the displacement of the ocean bottom, Inchin et al. (2022) use a tsunami model. Inchin et al. (2020) report three types of co-seismic perturbations of airglow. The first one is due to shock waves with dominant periods of ca. 60 s and vertical wavelengths of 17 km, which lead to a perturbation of up to 50% in the OH* airglow integrated volume emission rate and 15% in the OH(3-1) brightness weighted temperature. Second, they observe a quasi-permanent depletion in the volume emission rate; the authors speculate that this effect might last at least some minutes. Finally, they report airglow perturbations related to Rayleigh waves (acoustic waves that travel along the surface of solids) with periods of ca. 50 s leading to small perturbations of 1–5% in OH(3-1) integrated volume emission rate. Inchin et al. (2022) report that tsunamis causing an ocean surface displacement of 10 cm and higher result in acoustic and gravity waves, which lead to fluctuations in the OH(3-1) integrated volume emission rate of 1–17 % (see table 3 of the respective publication).

3.2.2 Infrasound or acoustic gravity waves in other measurements of the neutral atmosphere

Although the focus here is on the altitude range above 80 km, specifically on OH* airglow measurements, it should be noted that acoustic gravity waves and infrasound can also be detected at lower altitudes or by other measurement methods (stratospheric balloons: e.g., Garcia et al. (2022), Bowman et al. (2019), Bowman and Albert (2018), mesospheric radar: e.g., Belova et al. (2023), astronomical measurements of the airglow: Franzen et al. (2017)). In particular, following the 2022 Hunga-Tonga Hunga-Ha’apai (hereafter

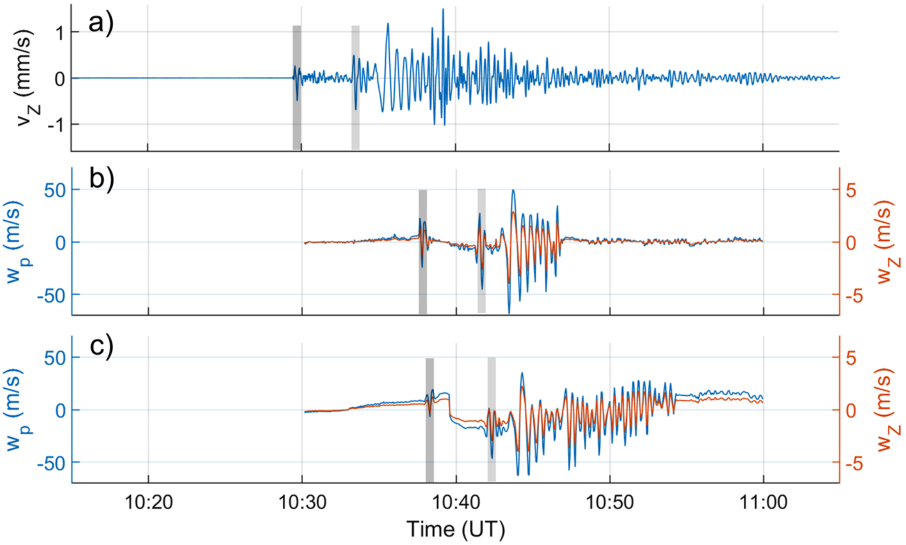

Fig. 8 Shown is the vertical component of the ground surface velocity v_z measured in Panská Ves, Czech Republic on 6 February 2023 after the M = 7.7 Turkey earthquake (**a**). The vertical plasma velocity w_p and the air particle oscillation velocity w_z as they were derived from the Doppler measurements at two different frequencies are displayed in (**b**) and (**c**). The first pulse (around 10:29:40 UT in v_z, dark grey rectangle) corresponds to P seismic waves, the second one (around 10:33:32 UT in v_z, light grey rectangle) to S seismic waves. The variations with a period about 20 s are due to infrasound. The long-term variations (seen mainly in (**c**)) are due to TIDs, which are not related to the earthquake

Hunga-Tonga) volcanic eruption, Wright et al. (2022) reported evidence of atmospheric waves from the troposphere through to the edge of space by analysing radiance data from various satellites. These included 10.3 μm emissions corresponding to tropospheric brightness temperatures as measured by the Geostationary Operational Environmental Satellites (GOES) (Schmit et al. (2017)), and 4.3 μm and 15 μm emissions associated with CO_2 absorption bands corresponding to stratospheric brightness temperatures from the Atmospheric Infrared Sounder (AIRS) on NASA's Aqua satellite and the Infrared Atmospheric Sounding Interferometer (IASI) on ESA's MetOp satellites (Hoffmann et al. (2014)).

Evidence of perturbations in the neutral atmosphere following the 2022 Hunga-Tonga volcanic eruption was also observable at thermospheric altitudes. Vadas et al. (2023) showed observations of large-scale thermospheric wind changes associated with gravity waves excited by the eruption. These measurements were taken by the Michelson Interferometer for Global High-Resolution Thermospheric Imaging (MIGHTI) on the Ionospheric Connection Explorer (ICON) satellite (Immel et al. (2018), Immel et al. (2023)), which captures horizontal neutral wind profiles between ~90–300 km. Li et al. (2023) showed neutral density perturbations following the eruption using in situ thermospheric density measurements from accelerometers onboard the Gravity Recovery and Climate Experiment (GRACE, Tapley et al. (2004)), Gravity Recovery and Climate Experiment Follow-On (GRACE-FO, Landerer et al. (2020)), and Swarm constellations (Olsen et al. (2013)).

3.3 Ionospheric Signatures of Waves Caused by Natural Hazards

Thanks to the wide availability of sensing techniques and instruments, the ionosphere has been extensively studied to identify waves induced by different natural hazards. Over the past appr. 60 years, numerous studies have investigated TIDs that highlight the underlying neutral waves. Other ionospheric phenomena associated with natural hazards, such as ionospheric holes (e.g., Astafyeva et al. (2013), Aa et al. (2022)) and changes to large-scale ionospheric structure and dynamics (e.g., Harding et al. (2022), Aa et al. (2022)), remain less well understood and characterized.

Earthquakes are known to generate different types of waves at the ground, which can be divided into body and surface waves. Surface waves include among others Rayleigh waves, while body waves are subdivided into primary (P) and secondary (S) waves (see Fig. 7). Earthquake-induced atmospheric waves have different sources such as co-seismic crustal displacement and Rayleigh seismic waves (Astafyeva et al. (2009), Astafyeva (2019)). The ionospheric signature caused by crustal displacement consists of acoustic waves that can be detected 7–9 min after the main shock, and are the result of ground shaking above the epicentre (Afraimovich et al. (2001), Astafyeva and Heki (2009), Heki and Ping (2005), Zettergren and Snively (2015), Inchin et al. (2020c), Inchin et al. (2021)). Rayleigh waves, which propagate along the Earth's surface, also generate acoustic waves as they travel, leading to detection in the ionosphere 7–9 min after their passage (Astafyeva et al. (2009), Kakinami et al. (2013), Haralambous et al. (2023), Alfonsi et al. (2024), Rolland et al. (2011)). For strong earthquakes, ionospheric signatures of P and S seismic waves can be observed at distances larger than about 2,000 km from the epicentre (e.g., Haralambous et al. (2023), Chum et al. (2012)) as demonstrated in Fig. 8, which shows the high-frequency (HF) Doppler observations of P, S, and Rayleigh wave ionospheric signatures caused by the 2023 earthquake in Turkey. Co-seismic crustal displacement and Rayleigh seismic waves typically produce N-shaped acoustic shock waves. However, Rayleigh waves are defined by linear propagation, whereas crustal displacement induced atmospheric waves may exhibit nonlinear effects (Inchin et al. (2020c), Inchin et al. (2021)).

The first detection of co-seismic ionospheric disturbances (CSIDs) was by Davies and Baker (1965), who used a Doppler sounder to detect the ionospheric signature of the Mw 9.2 Alaska earthquake of 1964. This earthquake was later detected in ionosonde measurements by Leonard and Barnes (1965). Since then, many studies have used Doppler sounders and ionosondes to investigate CSIDs (e.g., Maruyama et al. (2012), Maruyama et al. (2016), Chum et al. (2016), Chum et al. (2016b), Haralambous et al. (2023)). It was only 30 years later, with the advent of satellite-based navigation, that CSIDs were detected through their TEC signatures. Specifically, Calais and Minster (1995) were the first to use GNSS-derived TEC to study the Mw 6.7 Northridge earthquake. Since that first study, TEC has become the most widely used technique for studying earthquakes through their impact on the ionosphere, largely due to the extensive availability and spatial coverage of GNSS receivers (currently, there are tens of thousands of GNSS receivers worldwide, or even billions when considering smartphones). There is a fundamental difference between HF Doppler observations and TEC observations. HF Doppler sounding provides information on wave amplitude and phase at specific heights, which can be determined from nearby ionospheric sounders (ionograms), whereas GNSS TEC measurements provide integrated information on electron density variations along the entire line of sight between the GNSS receiver and the GNSS satellite, and additional assumptions about the height of the perturbation are required.

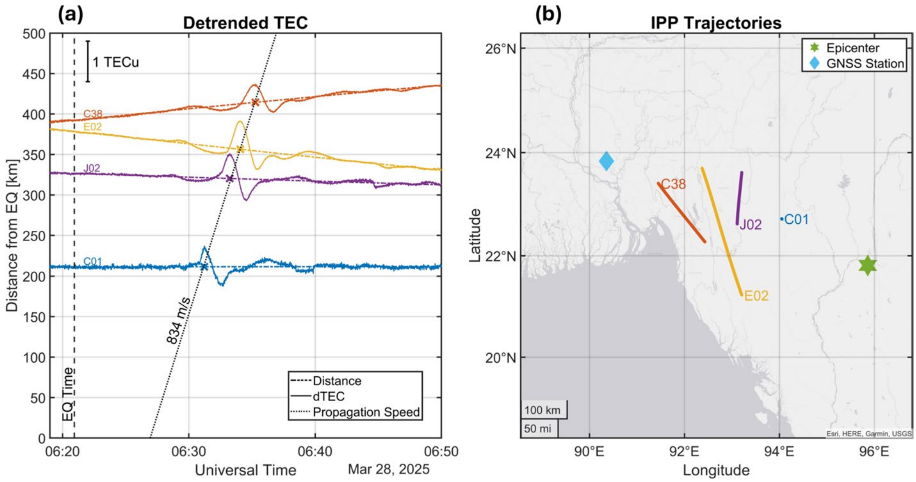

Fig. 9 Shown are the detrended differential total electron content (dTEC) perturbations derived from the GNSS satellites C01, J02, E02 and C38, and their ionospheric piercing point (IPP) trajectories, for the Myanmar earthquake on 28 March 2025. Panel **a** is a time-distance plot, with distance denoting the great-circle distance from the earthquake's epicentre. The crosses mark the times of the respective maxima; the gradient of their linear fit yields a propagation speed of 834 m/s. This value is consistent with the typical speed of the near-field ionospheric response to earthquakes. The vertical line indicates the time of the earthquake. Panel **b** shows the ground tracks of the four receiver-satellite links. The location of the GNSS station (in Dhaka, Bangladesh) is provided by the cyan diamond, and the green star indicates the epicentre location

The near-field ionospheric response shows TIDs propagating with speeds of around 600–1000 m/s, depending on the distance from the epicentre, and is attributed to acoustic-gravity waves from the piston-like motion of the crust. Figure 9 shows an example of such a near-field response to the Myanmar Mw 7.7 earthquake on March 28, 2025, where a 4-minute N-shaped TID is visible in dTEC measurements propagating at around 850 m/s away from the earthquake epicentre. The Rayleigh wave ionospheric signature, on the other hand, travels at the speed of the generating seismic wave, approximately 3–4 km/s. Typically, Rayleigh wave signatures are detectable at greater distances from the epicentre. Sometimes, P and S waves signatures can also be detected.

The ionospheric signatures of earthquakes usually have periods shorter than approximately 10 min and can be detected up to distances exceeding 9,000 km from the epicentre (Chum et al. (2012)). They may also provide information on the earthquake's focal mechanism (deformation in the source region), fault rupture propagation, and tsunamigenic potential (Astafyeva (2019)). Additionally, some studies have shown a linear relationship between earthquake magnitude and the strength of the ionospheric signature (Astafyeva et al. (2013), Cahyadi and Heki (2015)).

As summarized by Astafyeva (2019), some open questions remain regarding the direct relationship between wave shape and the focal mechanism. Moreover, for TEC studies, the mutual orientation of the GNSS receiver-satellite line of sight, the wave vector, and the magnetic field direction significantly affect the detected amplitude (Bagiya et al. (2019), Rolland et al. (2011), Rolland et al. (2013)). In addition, the detected amplitude is also influenced by the fault rupture propagation, as it can cause constructive or destructive wave interference (Bagiya et al. (2023), Inchin et al. (2020c), Inchin et al. (2021)). If the initial amplitude is large enough, nonlinear effects play an important role on wave propagation. In such a case, at altitudes where the oscillation velocity becomes comparable to the sound speed and/or the density perturbations become comparable to the background density (usually at high altitudes where the wave amplitude increases due to the decrease in air density), the shape and the spectral content of the original wave packet are changed due to nonlinear effects; this often leads to a formation of an N-shape perturbation (Chum et al. (2016, 2018)).

Similarly to earthquakes, the sea surface displacement caused by the propagation of tsunamis excites internal gravity waves that propagate obliquely to ionospheric heights (Inchin et al. (2020)). Due to the amplification of atmospheric waves, a tsunami wave that is even only a few centimetres tall can induce detectable signatures at ionospheric heights. The typical delay for these atmospheric waves to reach the ionosphere is around 45–60 min, which is probably too long for most early warning purposes. They are therefore not discussed further in this manuscript.

Volcanic eruptions can also excite gravity and acoustic waves (Astafyeva (2019)). Volcanic eruptions are generally classified as either effusive, characterized by the emission of hot lava, or explosive, which involves the abrupt release of large amounts of ash and gases. It is explosive eruptions that typically produce discernible atmospheric disturbances, including infrasound and gravity waves that can reach ionospheric heights. The pressure disturbances caused by explosive volcanic eruptions can be detected at ionospheric altitudes approximately 10–45 min after the eruption onset, and they often appear as quasi-periodic oscillations. Before the advent of TEC measurements, the first detection of the ionospheric signatures were performed through ionosondes (Igarashi et al. (1994)) or Doppler sounders (Liu et al. (1982), Cheng and Huang (1992)) for the 1991 Pinatubo and 1980 Mount Saint Helen eruptions. The first TEC-based detection was conducted by Heki (2006), who studied the ionospheric response to the 1 September 2001 eruption of the Asama volcano, identifying signatures of shock-acoustic waves approximately 12 min after the eruption onset, travelling at a speed of approximately 1.1 km/s. Subsequent studies investigated other eruptions, such as the 13 July 2003 Soufrière Hills volcano (Dautermann et al. (2009), Dautermann et al. (2009)), the 13 February 2014 Kelud volcanic explosion (Nakashima et al. (2016)), the April 2015 Calbuco eruptions (Liu et al. (2017), Shults et al. (2016), Tyska et al. (2024)), and the 10 April 2023 Shiveluch volcano (Riabova and Shalimov (2024)). On 15 January 2022, the strongest volcanic eruption since the 1991 Pinatubo event occurred at the island of Hunga-Tonga in the Pacific Ocean. This extreme event generated a wide range of atmospheric disturbances that have been extensively studied by the scientific community (Cahyadi et al. (2024), Liu et al. (2023), Themens et al. (2022), Maletckii and Astafyeva (2022), Ravanelli et al. (2023), Madonia et al. (2023), Figueiredo et al. (2023), Astafyeva et al. (2022a), Verhulst et al. (2022), Wright et al. (2022), Carter et al. (2023), Chum et al. (2023)). Ionospheric disturbances were also detected in the conjugate hemisphere following this event, likely due to magnetic-field aligned mapping of ionospheric electric fields generated by the neutral-wind driven dynamo (Gasque et al. (2022), Yamazaki et al. (2022), Iyemori et al. (2022), Shinbori et al. (2022)). There are still open questions regarding the different mechanisms responsible for generating these atmospheric waves, as the processes involved are not yet fully understood.

In addition to TIDs produced via the direct coupling between the neutral atmosphere and ionosphere, strong earthquakes and volcanic eruptions have been associated with various other ionospheric signatures. One of these, ionospheric depletions or ‘holes’ sometimes observed over the epicentre, has been suggested by Kamogawa et al. (2016) as an additional tool for the detection of tsunamis generated by earthquakes or volcanic eruptions. Ionospheric holes were first reported in the aftermath of the 2011 Tohoku underwater earthquake, when a plasma density depletion of several TEC units formed over the earthquake's epicentre and persisted for nearly an hour (Saito et al. (2011), Tsugawa et al. (2011)). Kakinami et al. (2012) reported ionospheric depletions over the underwater Chilean (2010) and Sumatran (2004) earthquakes, with both depletions persisting for 10 s of minutes. Initially, it was suggested that these ionospheric depletions occur only after undersea earthquakes that have associated tsunamis (Kakinami et al. (2012)). However, subsequent studies revealed evidence that this phenomenon can also occur following major inland earthquakes as well (Kamogawa et al. (2015), Sun et al. (2016)). Evidence suggests that the depth and duration of the depletion roughly scales with the earthquake's magnitude (Astafyeva et al. (2013)). Simulation studies suggest that nonlinear acoustic waves interacting with ionospheric plasma likely played a dominant role in depleting ionospheric plasma following the 2011 Tohoku earthquake (Shinagawa et al. (2013), Zettergren et al. (2017), Zettergren and Snively (2019)). Following the Hunga-Tonga eruption, an ionospheric hole was reported for the first time in connection with a volcanic eruption. Observations in the eruption's near-field showed a deep plasma density depletion (> 10 TEC units), which began forming within 45 min after the eruption (Aa et al. (2022), Astafyeva et al. (2022), Sun et al. (2022), He et al. (2023), Choi et al. (2023)). Compared to all ionospheric depletions observed after earthquakes to date, the depletion following the 2022 Tonga volcanic eruption was deeper, more spatially extensive, and longer-lasting (Aa et al. (2022); Astafyeva et al. (2022)).

4 Use of Atmospheric Waves for Early Warning Systems

In the context of natural hazards, every second counts, making real-time detection and characterization algorithms crucial. Once the data basis has been established, the challenge is to differentiate between atmospheric waves and/or TIDs generated by natural hazards and those that exist for other reasons. So, the algorithms do not only have to operate in real time or near real time (NRT), they also have to be robust against false alarms or missed detections. Achieving the right balance between accuracy and processing speed is essential. Moreover, the best approach probably involves using multi-instrument methodologies, combining different measurements, models, and expertise across disciplines.

Research in the context of early warning systems (EWS) is more advanced in the ionosphere than in the neutral part of the UMLT. This is despite the fact that the latter is closer to the source and therefore the propagation of the atmospheric waves emitted by natural hazards is less influenced by the respective atmospheric background. The reason is rather the availability of suitable measurement data. In particular, GNSS satellites provide nearly global coverage.

4.1 Early Warning System: Current Progress and Ideal State

In order to construct an early warning system, fast atmospheric waves (infrasound or acoustic gravity waves) and/or their corresponding TIDs generated by natural hazards need to be detected and appropriately characterised.

As mentioned above, the kind of data coverage that is possible with GNSS satellites in the ionosphere is currently not available for any other measurement system addressing higher altitudes. Although OH* airglow measurements from satellites are possible and have been done, a single or a few satellites are not helpful here; it would have to be a constellation of satellites with vast spatial coverage.

Concerning TID detection in NRT, a system capable of providing reliable dTEC data in real time is essential. Here, one must remember that atmospheric signatures have a natural delay relative to the originating source as neutral waves have to the respective heights to be detected. As a result, the concept of "real time" in ionospheric studies differs from ground-based techniques measuring surface variables. Currently, there is no strict standard definition for NRT in this context, as different neutral waves exhibit varying delays. At present, the NASA-JPL GUARDIAN system is the only system designed to provide such measurements for early warning purposes. As shown in Martire et al. (2022), GUARDIAN operates with TEC data from 70 GNSS receivers located over the so-called ring of fire. While GUARDIAN lacks automated detection and characterization modules, these are planned for future implementation. Other proposed NRT approaches and observables include VARION (Savastano et al. (2017), Savastano et al. (2019)), NeQuick calibrated GFLC (Guerra et al. (2024)), and the RTCM NTRIP-based technique by Maletckii and Astafyeva (2021). Savastano et al. (2017) demonstrated that VARION's NRT observables perform comparably to post-processed slant products. Guerra et al. (2024) introduced an observable that projects slant TEC to the vertical with minimal error, while Maletckii and Astafyeva (2021) noted that filtering or detrending TEC increases NRT delay and induces boundary errors. To address this, they considered TEC derivative time series.

After establishing available NRT observables and systems, the next focus is the autonomous identification of fast atmospheric waves and/or TIDs generated by natural hazards.

As pointed out in the former section, there only exist some case studies for the OH* airglow. For the ionosphere, several detection methods have already been employed, ranging from deep learning to more traditional techniques such threshold or statistical approaches. They could also serve, at least in part, as a suggestion for future airglow detection techniques. Yang et al. (2017) developed the first method for detecting multiple MSTIDs in differential TEC (dTEC) measurements from the GEONET network in Japan. Yang and Moreno et al. (2019) demonstrated the technique's ability to detect various superimposed TIDs, including those following the 2011 Tohoku-Oki earthquake. Lin (2022) introduced a method using generalized two-dimensional principal component analysis that detected a weak 11 cm tsunami. The advent of machine learning has led to the testing of new approaches, such as the random forest method by Brissaud and Astafyeva (2022), which detects co-seismic TIDs, picks arrival times, and associates detections across different satellites in NRT. Luhrmann et al. (2022) applied a similar technique but used long short-term memory (LSTM)-based anomaly detection. Fuso et al. (2024) and Ravanelli et al. (2024) employed gradient boosting and convolutional neural networks, respectively, to differentiate between quiet conditions (noise) and earthquake signatures and to retrieve arrival times. Despite these advancements, none of these techniques have been implemented in real-time systems, only in post-processing.

Once a TID is identified, the next step is determining the onset time and source location. Various techniques have been applied to earthquakes, tsunamis, and volcanic eruptions. Source location studies typically involve visually identifying TID arrival times, but integrating machine learning models could improve automation and NRT applicability. Afraimovich et al. (2006) were the first to propose a method for determining CSID speed and source from TEC measurements, followed by Kiryushkin and Afraimovich (2007), who applied a similar method to tsunami-induced TIDs. Subsequent studies (Liu et al. (2010), Liu et al. (2020), Lee et al. (2018), Tsai et al. (2011), Astafyeva and Shults (2019)) gave comparable results. Notably, Astafyeva et al. (2013)

used 1 Hz TEC data to locate the maximum crustal uplift caused by the Tohoku-Oki earthquake and tsunami and revealed the multi-segment structure of the seismic fault. As stronger earthquakes do not necessarily have epicentres coinciding with the maximum crustal uplift, their findings have crucial implications. Additionally, Astafyeva and Shults (2019) applied ray-tracing techniques to account for the vertical propagation of neutral waves. Knowing the precise magnitude and location of seafloor uplift is essential for reliable tsunami EWS. Maletckii and Astafyeva (2021) developed the first NRT 1 Hz interferometry-based technique for detecting and characterizing TID induced by natural hazards and other sources, including solar flares, rocket launches, typhoons, and man-made explosions. In subsequent years, they adapted their algorithm for 30-second data (Maletckii and Astafyeva (2022), Maletckii et al. (2023)), increasing delay times from 15 to 30 min, while also introducing a module that distinguishes between different sources using a TID dictionary (Maletckii and Astafyeva (2024)).

The final step in developing an accurate EWS is determining source parameters based on responses of the neutral or ionized atmosphere. The most commonly used parameter for evaluating earthquake strength is magnitude. Occhipinti et al. (2018) demonstrated that Rayleigh wave signatures detected by over-the-horizon radars and Doppler sounders could estimate earthquake magnitude with precision comparable to a single seismometer. Ionospheric studies, however, offer unique insights into source characterization, particularly for large earthquakes where multiple faults are activated, and crustal displacement is difficult to estimate until synthetic aperture radars provide data (typically with a three-day delay) or results from advanced source models are available. Additionally, estimating the tsunami potential based on seismic responses is challenging and often leads to false alarms, as earthquake magnitude is affected by crustal rigidity and fault size. The ionospheric response, in contrast, directly correlates with crustal displacement. Astafyeva and Heki (2009) suggested that the spatial distribution of N- and inverted N-shapes could help deduce focal mechanisms, while Astafyeva et al. (2013) found a correlation between the amplitude and duration of negative N waves and crustal displacement. Kamogawa et al. (2016) aimed to estimate initial tsunami height using the amplitude of the near-field TEC depression rates, providing results within 20 min of the event. Manta et al. (2020) further refined this approach by focusing on displaced volume rather than uplift, revealing a strong correlation between their wave activity index and tsunami potential.

Finally, recent studies (Rakoto et al. (2018), Komjathy et al. (2016)) have demonstrated the ability to use coupled atmosphere–ionosphere models to derive tsunami wave height with centimetre-level precision, which is particularly useful for far-field events. GNSS receivers, being more widespread and cost-effective than buoys, offer a practical solution for future tsunami warning systems. Volcanic eruptions remain more complex, but Manta et al. (2021) found that ionospheric response amplitudes for stronger eruptions correlate with the volcanic explosive index and plume height.

4.2 Challenges and Requirements

The previous subsection looked at the current state of EWS and promising efforts. This subsection identifies the challenges. Due to the better data coverage, the challenges for the ionospheric part relate to data analysis and subsequent steps, whereas for OH* airglow measurements they cover a wider range.

The ionosphere is a highly variable medium, influenced from both below and above. Ionospheric models can help to understand this variability; however, a number of phenomena still leads to deviations from the expected state. A key aspect in estimating the amplitude of TIDs is understanding the background ionospheric conditions, particularly the electron density profile (EDP). Due to the coupling of the near-Earth environment with the solar wind, geomagnetic storms are known to induce both positive (increasing electron density) and negative (decreasing electron density) effects on the ionospheric density. Moreover, geomagnetic storms can trigger large-scale TIDs that propagate from auroral to equatorial latitudes and occasionally extend into the opposite hemisphere (Habarulema et al. (2015)). Since large-scale TIDs (LSTIDs) generally exhibit longer periods than those induced by natural hazards, filtering techniques should be employed with adequate precautions to minimize the impact of these disturbances and the effects of filtering artefacts. In addition to geospace forcing, other types of disturbances in the ionosphere may hinder the identification and accurate characterization of medium-scale TIDs (MSTIDs) such as those produced by the solar terminator, which are similar to volcano and tsunami-induced MSTIDs. To reduce the likelihood of false alarms, a comprehensive understanding of MSTID climatology is essential, and an ionospheric EWS should be integrated into pre-existing hazard monitoring frameworks.

The ionosphere may also react differently to natural hazards during the day and at night. For example, clear co-seismic signatures were detected in the ionosphere for the daytime M7.7 Turkey earthquake on 6 February 2023, whereas no significant response was observed in the ionosphere for the preceding M7.8 shock at night on the same day (Haralambous et al. (2023)). However, this result cannot be generalized as there are many observations of nighttime co-seismic disturbances in the ionosphere for other earthquakes. It should also be noted that the dynamics of the ionosphere is different for low, mid and high latitudes.

Another aspect is that the movement of Global Navigation Satellite System (GNSS) satellites introduces Doppler effects on the detected TID signal, particularly in the case of low-elevation satellites (Guerra et al. (2024)). One potential solution is the use of geostationary (GEO) satellites (Savastano et al. (2019)), as their fixed ionospheric detection points eliminate the impact of ionospheric pierce point (IPP) movement. With the increase in space-based instruments, such as radio occultation measurements (Coïsson et al. (2015)), in situ electron density measurements (Verhulst et al. (2022)), new frontiers in the ionospheric detection of natural hazards will open (Komjathy et al. (2016)), as they will cover areas of the ionosphere that are not currently tracked, such as over oceans. Unlike TEC measurements, Doppler measurements are not subject to geometrical and integration effects, as they can probe different heights and densities of the ionosphere by varying the frequency of the transmitted signal.

Finally, the background atmosphere influences natural hazard induced signatures not only in the ionosphere but also the neutral part of the UMLT. When determining the source of a neutral wave, the (horizontal) background wind velocity plays a critical role in the wave vertical propagation speed and its direction. While atmospheric models are typically used to account for this, the atmosphere's inherent variability introduces the potential for estimation errors. Additionally, when employing TEC measurements, geometrical and integration effects can affect both the amplitude and timing of TID estimations. To address these issues, models that account for non-tectonic forcing and the altitude of ionospheric disturbances may provide a solution (Bagiya et al. (2019)). Nonetheless, the real-time use of such models is computationally demanding, and considering the time-sensitive nature of EWS, these models must be computationally efficient while maintaining a high degree of reliability.

The challenges of detecting atmospheric waves generated by natural hazards also exist for OH* airglow measurements. However, there is also a lack of suitable data here. So, first of all, the data basis needs to be enhanced. Otherwise, algorithms for the identification and characterization of atmospheric waves induced by natural hazards cannot be further developed and tested. In the following, some important aspects concerning the parameters derived by OH*-airglow measurements and the choice of the field of view of an airglow imager will be given (Fig. 10).

As the signal is averaged over the OH*-airglow layer for ground-based and spaceborne nadir instruments, these measurements are not sensitive to all vertical wavelengths. The averaging depends on the thickness and form of the OH*-airglow layer (e.g., Swenson and Gardner (1998), Wüst et al. (2016)). At least the first shows some temporal variation (e.g., Shepherd et al. (2006), von Savigny (2015), Wüst et al. (2017b, 2020)). Due to the residual circulation, which transports atomic oxygen needed for the formation of OH* vertically, the OH*-airglow layer is on average thinner in summer than in winter (by roughly 1–2 km for the Alpine region, see Fig. 11).

This is of interest when looking for infrasound with periods of ca. 25 s and less at least directly above a source (see Fig. 10). The longer the period, the less averaging effects due to the vertical extension of the OH*-airglow layer play a role. Slant propagation paths improve the situation. OH* measurements deliver airglow intensities. Based on calculations of the vertical averaging effect, Swenson and Gardner (1998) showed that it is not only sufficient but also preferable to work with the airglow intensity measurements instead of the temperatures in this case. So, the extra step from intensity to temperature can and should be avoided.

As discussed above, in the gravity wave branch only acoustic gravity waves with an intrinsic period very near to the Brunt-Väisälä period can be used in the context of early warning. These waves have short horizontal wavelength in the range of tens of km (see Figs. 12 and 13). Their vertical wavelength is long compared to waves with the same horizontal wavelength but larger periods (see Fig. 12), which makes vertical averaging

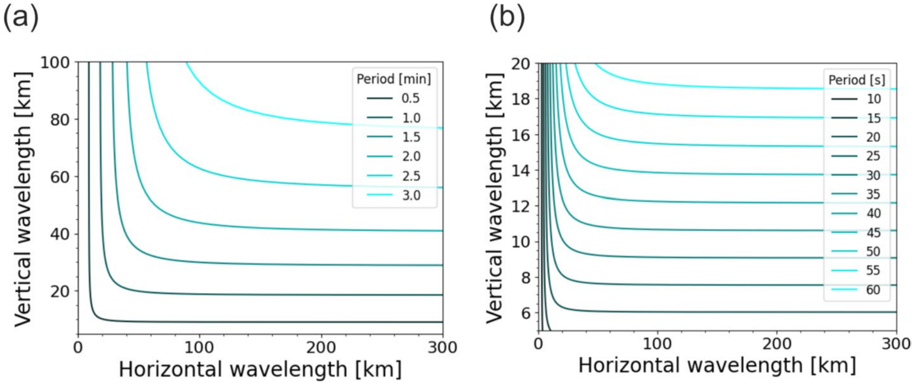

Fig. 10 The calculation of this figure is based on Eq. (3); however, here different periods typical for infrasound are used (a: 0.5–3 min, b: 10–60 s). Due to vertical averaging effects, the shortest periods will probably not be detectable in OH*-airglow measurements. The calculation refers to infrasound that is propagating purely vertically

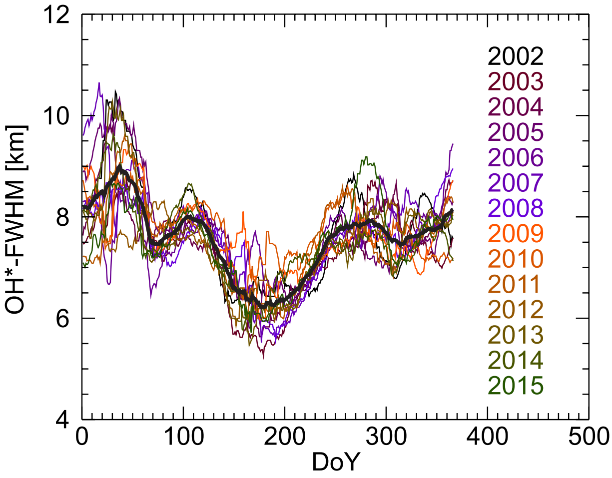

Fig. 11 Shown is smoothed yearly course of the full-width at half maximum (FWHM) of the OH* airglow layer derived from TIMED-SABER measurements over the Alpine region for the years 2002–2015. The black line is the average over all years. Reprinted under CC-BY−4.0 license from Wüst et al. (2017b) ©2017, The Author(s)

effects due to the thickness of the OH*-airglow layer less important. However, in these cases the horizontal wavelengths are in the range of a few kilometres only, which needs to be taken into account for the spatial resolution of imaging systems and the choice of the analysis method. To reach the OH*-airglow layer with its centroid height around 85–87 km after ca. 15 min, a vertical phase velocity of at least 96 m/s is needed. This is comparatively fast for gravity waves (see, e.g., figure 5 of Nakamura et al. (1999), figure 4 of Suzuki et al. (2004), figure 4 of Wachter et al. (2015) or figure 2 (b) of Wüst et al. (2018)) and only a small part of the spectrum of acoustic gravity waves satisfies it (see Fig. 13). Furthermore, the background atmosphere, through which the gravity waves propagate upwards, plays a role. Tropospheric and stratospheric jets have typical wind speeds of approximately 15 and 60 m/s. Only waves with horizontal phase speeds faster than 60 m/s or whose phase velocity is opposite to the direction of the corresponding jets can reach the height of the OH*-airglow layer.

The situation changes for infrasound: while the vertical wavelength and therefore also the vertical phase speed of acoustic gravity waves change for a fixed period with the horizontal wavelength, (see Fig. 12), the vertical wavelength stays constant for a fixed infrasound period over a large range of horizontal wavelengths (see Fig. 10).

These considerations set important boundary conditions for the choice of the field of view and the spatial resolution of an OH*-airglow imager. Finally, one restrictive natural aspect should be mentioned. OH*-airglow measurements, as carried out in the vast majority of cases today, have the disadvantage that they are only made at night. Daytime measurements have been demonstrated from the ground (Sridharan et al. (1998)) and require narrow-band filters. However, the height, width and shape of the OH*-airglow layer changes during the day due to solar radiation and the associated chemical processes: the OH* dayglow is characterised by a double peak structure with the upper layer at a similar height as in the case of the OH* nightglow and the lower layer between 70 and 85 km, increasing with the time of day (Gao et al. (2015)). Other dayglow emissions might be useful here.

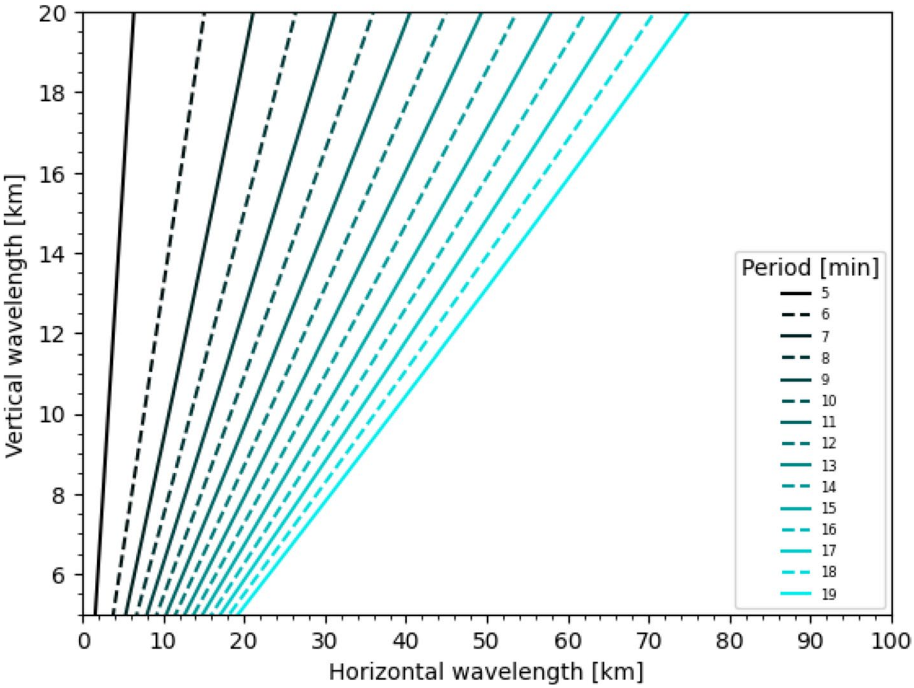

Fig. 12 According to the dispersion relation for acoustic gravity waves (see Eq. (3)) the vertical wavelength increases with the horizontal wavelength. This holds for every intrinsic period. For simplification, the background wind is set to zero, so the intrinsic period equals the (observed) period. Imaging system with a field of view of some 10 km are suitable for the detection of these acoustic gravity waves. OH*-airglow spectrometers, which typically average over some km to some 10 km, will probably only detect the longer-periodic part of the acoustic gravity wave spectrum shown here

5 Summary and Conclusion

It has long been known that atmospheric waves can propagate both horizontally and vertically over great distances in the atmosphere. The idea of using atmospheric waves generated by natural hazards such as tsunamis to help early warning of those hazards has been discussed since at least the 1970s. In particular, when the measurement takes place at higher altitudes, e.g. above 80 km, as considered in this manuscript, atmospheric waves that can propagate vertically within a few minutes are most suitable for this purpose. For this reason, the focus needs to be on infrasound and acoustic gravity waves in this case.

For heights above 80 km, the neutral atmosphere and the ionosphere co-exist. Nevertheless, research on atmospheric waves induced by natural hazards and their use for early warning is much more advanced for the ionosphere (based here on GNSS, Doppler and digisondes) than for the neutral gas atmosphere considered around 90 km height (based here on OH*-airglow measurements). This is mainly due to the availability of satellite-based GNSS measurements with its unique coverage compared to all other height regions. Both communities face similar challenges: the correct differentiation of atmospheric signals induced by natural hazards from those of other sources, and the influence of the background atmosphere on the propagation and the observed wave parameters to name just two. To some extent, atmospheric models can help by simulating the expected propagation. And

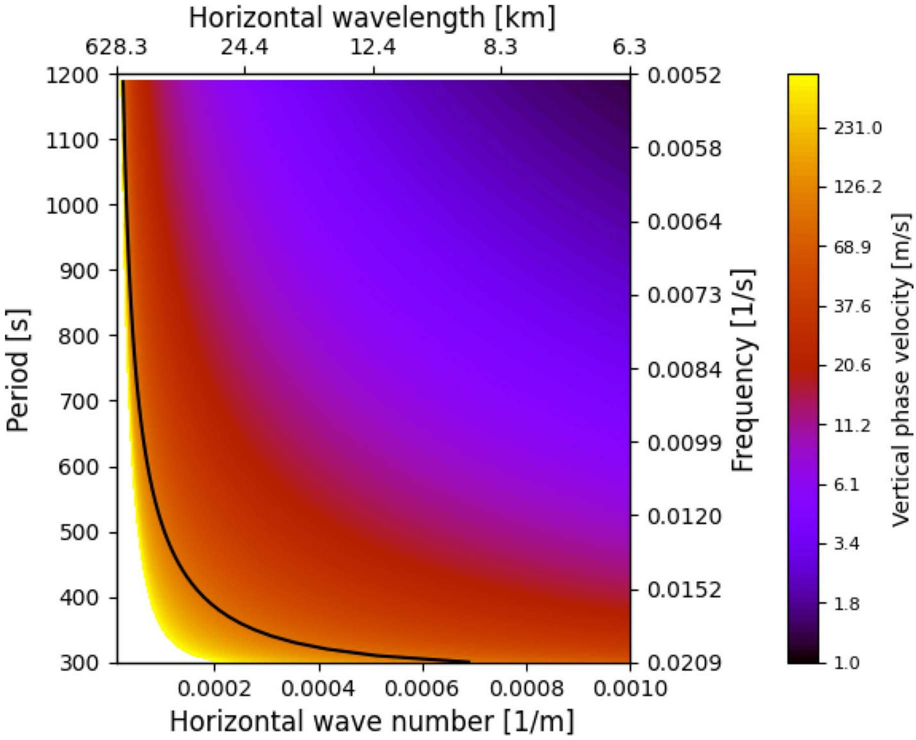

Fig. 13 The period (frequency) of acoustic gravity waves is plotted versus the horizontal wave number (wavelength), the vertical phase velocity is colour coded. The solid line refers to a vertical phase velocity of 95.6 m/s, which is the minimal velocity to reach 86 km height within 15 min. Also in this case, the background wind is assumed to be zero

finally, both communities might profit from synergies as the different measuring methods are sensitive to specific parts of the atmospheric wave spectrum.

Just as cooperation within the atmospheric community is helpful, cooperation with other disciplines, such as seismologists in this case, could also provide further insights as early warning still is a central focus there. Fostering a multidisciplinary approach that brings together atmospheric scientists with seismologists could have a profound impact. Such collaboration would enable the mutual exchange of previously acquired knowledge, techniques, and ideas, allowing each field to benefit from the other's expertise. Seismologists' well-established methodologies for real-time event characterization, data assimilation, and signal processing could be adapted to study post-earthquake neutral atmospheric and ionospheric disturbances. Conversely, neutral atmospheric and ionospheric scientists can contribute insights into how seismic energy propagates through the upper atmosphere, improving our understanding of earthquake-atmosphere coupling. By integrating expertise from the different disciplines, researchers can develop more comprehensive and reliable monitoring systems, enhancing global early warning capabilities and broadening the scope of earthquake impact assessment.

Acknowledgements This paper is an outcome of the workshop "Physical Links Between Weather and climate in Space and the Lower Atmosphere" held at the International Space Science Institute (ISSI) in Bern, Switzerland (22–26 January 2024). Sabine Wüst thanks ISSI for hosting the workshop and for providing accommodation in Bern to attend it. Furthermore, she thanks Lucilla Alfonsi (INGV) and Ruth Lieberman (NASA) for establishing the contact to Marco Guerra and Claire Gasque. Marco Guerra's PhD is funded by an INGV project named "Rete Multiparametrica" under the topic "Space Weather: PECASUS." This manuscript was linguistically improved by artificial intelligence (deepl.com). The authors thank the anonymous reviewers for the valuable comments.

Author Contributions SW had the idea for this manuscript, structured it and wrote the parts which refer to the neutral atmosphere. MG, JC and CG wrote the parts referring to the ionosphere. All authors read the manuscript.

Funding Open Access funding enabled and organized by Projekt DEAL.

Declarations

Conflict of interest The authors declare that they have no Conflict of interest.

References

Aa E, Zhang S-R, Erickson PJ, Vierinen J, Coster AJ, Goncharenko LP, Spicher A, Rideout W (2022) Significant ionospheric hole and equatorial plasma bubbles after the 2022 Tonga volcano eruption. Space Weather 20(7):2022–003101

Aa E, Zhang S-R, Wang W, Erickson PJ, Qian L, Eastes R, Harding BJ, Immel TJ, Karan DK, Daniell RE et al (2022) Pronounced suppression and X-pattern merging of equatorial ionization anomalies after the 2022 Tonga volcano eruption. J Geophys Res Space Phys 127(6):2022–030527

Afraimovich EL, Astafieva EI, Kirushkin VV (2006) Localization of the source of ionospheric disturbance generated during an earthquake. Int J Geomagn Aeron 6(2):2002. https://doi.org/10.1029/2004GI000092

Afraimovich EL, Perevalova NP, Plotnikov AV, Uralov AM (2001) The shock-acoustic waves generated by earthquakes. Ann Geophys 19(4):395–409. https://doi.org/10.5194/angeo-19-395-2001

Alexander M, Geller M, McLandress C, Polavarapu S, Preusse P, Sassi F, Sato K, Eckermann S, Ern M, Hertzog A et al (2010) Recent developments in gravity-wave effects in climate models and the global distribution of gravity-wave momentum flux from observations and models. Q J R Meteorol Soc 136(650):1103–1124. https://doi.org/10.1002/qj.637

Alfonsi L, Cesaroni C, Hernandez-Pajares M, Astafyeva E, Bufféral S, Elias P, Belehaki A, Ioanna T, Yang H, Guerra M (2024) Ionospheric response to the 2020 Samos earthquake and tsunami. Earth Planets Space 76(1):13. https://doi.org/10.1186/s40623-023-01940-2

Astafyeva E, Maletckii B, Mikesell TD, Munaibari E, Ravanelli M, Coisson P, Manta F, Rolland L (2022) The 15 January 2022 Hunga Tonga eruption history as inferred from ionospheric observations. Geophys Res Lett. https://doi.org/10.1029/2022GL098827

Astafyeva E, Rolland L, Lognonné P, Khelfi K, Yahagi T (2013) Parameters of seismic source as deduced from 1 Hz ionospheric GPS data: case study of the 2011 Tohoku-Oki event. J Geophys Res Space Phys 118(9):5942–5950. https://doi.org/10.1002/jgra.50556

Astafyeva E, Shalimov S, Olshanskaya E, Lognonné P (2013) Ionospheric response to earthquakes of different magnitudes: larger quakes perturb the ionosphere stronger and longer. Geophys Res Lett 40(9):1675–1681. https://doi.org/10.1002/grl.50398

Astafyeva E, Shults K (2019) Ionospheric GNSS imagery of seismic source: possibilities, difficulties, and challenges. J Geophys Res Space Phys 124(1):534–543. https://doi.org/10.1029/2018JA026107

Astafyeva E (2019) Ionospheric detection of natural hazards. Rev Geophys 57(4):1265–1288. https://doi.org/10.1029/2019RG000668

Astafyeva E, Heki K (2009) Dependence of waveform of near-field coseismic ionospheric disturbances on focal mechanisms. Earth Planets Space 61(7):939–943. https://doi.org/10.1186/BF03353206

Astafyeva E, Heki K, Kiryushkin V, Afraimovich E, Shalimov S (2009) Two-mode long-distance propagation of coseismic ionosphere disturbances. J Geophys Res Space Phys. https://doi.org/10.1029/2008JA013853

Astafyeva E, Maletckii B, Mikesell TD, Munaibari E, Ravanelli M, Coïsson P, Manta F, Rolland L (2022) The 15 January 2022 Hunga Tonga eruption history as inferred from ionospheric observations. Geophys Res Lett 49(10):2022–098827

Bagiya MS, Heki K, Gahalaut VK (2023) Anisotropy of the near-field coseismic ionospheric perturbation amplitudes reflecting the source process: the 2023 February Turkey earthquakes. Geophys Res Lett 50(14):2023–103931. https://doi.org/10.1029/2023GL103931

Bagiya MS, Sunil AS, Rolland L, Nayak S, Ponraj M, Thomas D, Ramesh DS (2019) Mapping the impact of non-tectonic forcing mechanisms on GNSS measured coseismic ionospheric perturbations. Sci Rep. https://doi.org/10.1038/s41598-019-54354-0

Bass H, Sutherland ELC, Piercy J, Evans L (1984) Absorption of sound by the atmosphere. Phys Acoust 17

Baumjohann W, Treumann RA (2012) Basic space plasma physics. World Scientific, Singapur

Belova E, Barabash V, Godin OA, Kero J, Näsholm SP, Vorobeva E, Le Pichon A (2023) High-speed echoes in the polar winter mesosphere: infrasound as a probable cause. Adv Space Res 72(8):3181–3201. https://doi.org/10.1016/j.asr.2023.07.010

Benioff H, Ewing M, Press F (1951) Sound waves in the atmosphere generated by a small earthquake. Proc Natl Acad Sci 37(9):600–603

Billingham J, King AC (2000) Wave motion. Cambridge University Press, New York

Bittner M, Höppner K, Pilger C, Schmidt C (2010) Mesopause temperature perturbations caused by infrasonic waves as a potential indicator for the detection of tsunamis and other geo-hazards. Nat Hazard 10(7):1431–1442. https://doi.org/10.5194/nhess-10-1431-2010

Blanc E, Pichon A, Ceranna L, Farges T, Marty J, Herry P (2009) Global scale monitoring of acoustic and gravity waves for the study of the atmospheric dynamics. In: Le Pichon A, Blanc E, Hauchecorne A (eds) Infrasound monitoring for atmospheric studies. Springer, Dordrecht, pp 647–664. https://doi.org/10.1007/978-1-4020-9508-5_21

Bock Y, Melgar D (2016) Physical applications of GPS geodesy: a review. Rep Prog Phys 79(10):106801. https://doi.org/10.1088/0034-4885/79/10/106801

Bowman D, Lees J, Cutts J, Komjathy A, Young E, Seiffert K, Boslough M, Arrowsmith S (2019) Geoacoustic observations on drifting balloon-borne sensors. In: Le Pichon A (ed) Infrasound monitoring for atmospheric studies. Springer, Cham, pp 125–171. https://doi.org/10.1007/978-3-319-75140-5_4

Bowman DC, Albert SA (2018) Acoustic event location and background noise characterization on a free flying infrasound sensor network in the stratosphere. Geophys J Int 213(3):1524–1535. https://doi.org/10.1093/gji/ggy069

Brissaud Q, Astafyeva E (2022) Near-real-time detection of co-seismic ionospheric disturbances using machine learning. Geophys J Int 230(3):2117–2130. https://doi.org/10.1093/gji/ggac167

Cahyadi MN, Heki K (2015) Coseismic ionospheric disturbance of the large strike-slip earthquakes in north sumatra in 2012: Mw dependence of the disturbance amplitudes. Geophys J Int 200(1):116–129. https://doi.org/10.1093/gji/ggu343

Cahyadi MN, Muslim B, Muafiry IN, Gusman AR, Handoko EY, Anjasmara IM, Putra ME, Wulansari M, Lestari DS, Jin S, Sri Sumantyo JT (2024) 3d traveling ionospheric disturbances during the 2022 Hunga Tonga-Hunga Ha'apai eruption using GNSS TEC. J Geophys Res Space Phys 129(3):2023–031806. https://doi.org/10.1029/2023JA031806

Calais E, Minster JB (1995) GPS detection of ionospheric perturbations following the January 17, 1994. Northridge Earthq Geophys Res Lett 22(9):1045–1048. https://doi.org/10.1029/95GL00168

Carter BA, Pradipta R, Dao T, Currie JL, Choy S, Wilkinson P, Maher P, Marshall R, Harima K, Le Huy M, Nguyen Chien T, Nguyen Ha T, Harris TJ (2023) The ionospheric effects of the 2022 Hunga Tonga volcano eruption and the associated impacts on GPS precise point positioning across the Australian region. Space Weather 21(5):2023–003476. https://doi.org/10.1029/2023SW003476

Cheng K, Huang Y-N (1992) Ionospheric disturbances observed during the period of Mount Pinatubo eruptions in June 1991. J Geophys Res Space Phys 97(A11):16995–17004. https://doi.org/10.1029/92JA01462

Choi J-M, Lin C, Rajesh P, Lin J-T, Chou M, Kwak Y-S, Chen S-P (2023) Giant ionospheric density hole near the 2022 Hunga-Tonga volcanic eruption: Multi-point satellite observations

Chum J, Cabrera MA, Mošna Z, Fagre M, Baše J, Fišer J (2016) Nonlinear acoustic waves in the viscous thermosphere and ionosphere above earthquake. J Geophys Res Space Phys 121(12):12126–12137. https://doi.org/10.1002/2016JA023450

Chum J, Hruska F, Zednik J, Lastovicka J (2012) Ionospheric disturbances (infrasound waves) over the Czech Republic excited by the 2011 Tohoku earthquake. J Geophys Res Space Phys. https://doi.org/10.1029/2012JA017767

Chum J, Liu J-Y, Podolská K, Šindelářová T (2018) Infrasound in the ionosphere from earthquakes and typhoons. J Atmos Solar Terr Phys 171:72–82. https://doi.org/10.1016/j.jastp.2017.07.022

Chum J, Liu J-Y, Laštovika J, Fišer J, Mošna Z, Baše J, Sun Y-Y (2016) Ionospheric signatures of the April 25, 2015 Nepal earthquake and the relative role of compression and advection for Doppler sounding of infrasound in the ionosphere. Earth Planets Space 68(1):24. https://doi.org/10.1186/s40623-016-0401-9

Chum J, Šindelářová T, Koucká Knížová P, Podolská K, Rusz J, Baše J, Nakata H, Hosokawa K, Danielides M, Schmidt C, Knez L, Liu J-Y, Molina MG, Fagre M, Katamzi-Joseph Z, Ohya H, Omori T, Laštovička J, Obrazová Burešová D, Kouba D, Urbář J, Truhlík V (2023) Atmospheric and ionospheric waves induced by the Hunga eruption on 15 January 2022; doppler sounding and infrasound. Geophys J Int 233(2):1429–1443. https://doi.org/10.1093/gji/ggac517

Coïsson P, Lognonné P, Walwer D, Rolland LM (2015) First tsunami gravity wave detection in ionospheric radio occultation data. Earth Space Sci 2(5):125–133. https://doi.org/10.1002/2014EA000054

Dautermann T, Calais E, Lognonné P, Mattioli GS (2009) Lithosphere–atmosphere–ionosphere coupling after the 2003 explosive eruption of the Soufriere Hills Volcano. Montserrat Geophys J Int 179(3):1537–1546. https://doi.org/10.1111/j.1365-246X.2009.04390.x

Dautermann T, Calais E, Mattioli GS (2009) Global Positioning System detection and energy estimation of the ionospheric wave caused by the 13 July 2003 explosion of the Soufrière Hills Volcano, Montserrat. J Geophys Res Solid Earth. https://doi.org/10.1029/2008JB005722

Davies K, Baker DM (1965) Ionospheric effects observed around the time of the Alaskan earthquake of March 28, 1964. J Geophys Res (1896-1977) 70(9):2251–2253. https://doi.org/10.1029/JZ070i009p02251

Ern M, Preusse P, Gille J, Hepplewhite C, Mlynczak M, Russell J III, Riese M (2011) Implications for atmospheric dynamics derived from global observations of gravity wave momentum flux in stratosphere and mesosphere. J Geophys Res Atmosp. https://doi.org/10.1029/2011JD015821

Figueiredo CAOB, Vadas SL, Becker E, Wrasse CM, Takahashi H, Nyassor PK, Barros D (2023) Secondary gravity waves from the Tonga volcano eruption: observation and modeling over New Zealand and Australia. J Geophys Res Space Phys 128(10):2023–031476. https://doi.org/10.1029/2023JA031476

Franzen C, Hibbins RE, Espy PJ, Djupvik AA (2017) Optimizing hydroxyl airglow retrievals from long-slit astronomical spectroscopic observations. Atmosp Meas Techn 10(8):3093–3101. https://doi.org/10.5194/amt-10-3093-2017

Fritts DC, Alexander MJ (2003) Gravity wave dynamics and effects in the middle atmosphere. Rev Geophys. https://doi.org/10.1029/2001RG000106

Fuso F, Crocetti L, Ravanelli M, Soja B (2024) Machine learning-based detection of TEC signatures related to earthquakes and tsunamis: the 2015 Illapel case study. GPS Solut 28(3):106. https://doi.org/10.1007/s10291-024-01649-z

Gao H, Xu J, Ward W, Smith AK, Chen G-M (2015) Double-layer structure of oh dayglow in the mesosphere. J Geophys Res Space Phys 120(7):5778–5787. https://doi.org/10.1002/2015ja021208

Garcia RF, Klotz A, Hertzog A, Martin R, Gérier S, Kassarian E, Bordereau J, Venel S, Mimoun D (2022) Infrasound from large earthquakes recorded on a network of balloons in the stratosphere. Geophys Res Lett 49(15):2022–098844. https://doi.org/10.1029/2022GL098844

Gasque LC, Wu Y-J, Harding BJ, Immel TJ, Triplett CC (2022) Rapid volcanic modification of the E-region dynamo: ICON's first glimpse of the Tonga eruption. Geophys Res Lett 49(18):2022–100825

Geller MA, Alexander MJ, Love PT, Bacmeister J, Ern M, Hertzog A, Manzini E, Preusse P, Sato K, Scaife AA, Zhou T (2013) A comparison between gravity wave momentum fluxes in observations and climate models. J Clim 26(17):6383–6405. https://doi.org/10.1175/JCLI-D-12-00545.1

Gossard E, Hooke W (1975) Waves in the atmosphere. Elsevier Scientific Publishing Company, Amsterdam, Netherlands

Guerra M, Cesaroni C, Ravanelli M, Spogli L (2024) Travelling ionospheric disturbances detection: A statistical study of detrending techniques, induced period error and near real-time observables. J Space Weather Space Clim 14:17. https://doi.org/10.1051/swsc/2024017

Habarulema JB, Katamzi ZT, Yizengaw E (2015) First observations of poleward large-scale traveling ionospheric disturbances over the African sector during geomagnetic storm conditions. J Geophys Res Space Phys 120(8):6914–6929. https://doi.org/10.1002/2015JA021066

Haider SA, Thirupathaiah P, Batista IS, Abdu MA, Sobral JHA, Gobbi D (2022) Modeling and causative mechanism of OI 6.300 nm nightglow emission over Cachoeira Paulista (22.7° S, 45° W) - Brazil: Seasonal and temporal variability. Adv Space Res 69(2):889–904. https://doi.org/10.1016/j.asr.2021.10.018

Hannawald P, Schmidt C, Wüst S, Bittner M (2016) A fast SWIR imager for observations of transient features in OH airglow. Atmosp Meas Techn 9(4):1461–1472. https://doi.org/10.5194/amt-9-1461-2016

Haralambous H, Guerra M, Chum J, Verhulst TGW, Barta V, Altadill D, Cesaroni C, Galkin I, Márta K, Mielich J, Kouba D, Buresova D, Segarra A, Spogli L, Rusz J, Zedník J (2023) Multi-instrument observations of various ionospheric disturbances caused by the 6 February 2023 Turkey earthquake. J Geophys Res Space Phys 128(12):2023–031691. https://doi.org/10.1029/2023JA031691

Harding BJ, Wu Y-JJ, Alken P, Yamazaki Y, Triplett CC, Immel TJ, Gasque LC, Mende SB, Xiong C (2022) Impacts of the January 2022 Tonga volcanic eruption on the ionospheric dynamo: ICON-MIGHTI and Swarm observations of extreme neutral winds and currents. Geophys Res Lett 49(9):2022–098577

Harrison RG, Aplin KL, Rycroft MJ (2010) Atmospheric electricity coupling between earthquake regions and the ionosphere. J Atmos Solar Terr Phys 72:376–381. https://doi.org/10.1016/j.jastp.2009.12.004

He J, Astafyeva E, Yue X, Ding F, Maletckii B (2023) The giant ionospheric depletion on 15 January 2022 around the Hunga Tonga-Hunga Ha'apai volcanic eruption. J Geophys Res Space Phys 128(1):2022–030984

Heki K (2006) Explosion energy of the 2004 eruption of the Asama Volcano, central Japan, inferred from ionospheric disturbances. Geophys Res Lett. https://doi.org/10.1029/2006GL026249

Heki K, Ping J (2005) Directivity and apparent velocity of the coseismic ionospheric disturbances observed with a dense GPS array. Earth Planet Sci Lett 236(3):845–855. https://doi.org/10.1016/j.epsl.2005.06.010

Hines CO (1960) Internal atmospheric gravity waves at ionospheric heights. Can J Phys 38(11):1441–1481. https://doi.org/10.1139/p60-150

Hines CO (1972) Gravity waves in the atmosphere. Nature 239(5367):73–78. https://doi.org/10.1038/239073a0

Hocke SKK (1996) A review of atmospheric gravity waves and travelling ionospheric disturbances: 1982–1995. Ann Geophys 14:917–940. https://doi.org/10.1007/s00585-996-0917-6

Hoffmann L, Alexander MJ, Clerbaux C, Grimsdell AW, Meyer CI, Rößler T, Tournier B (2014) Intercomparison of stratospheric gravity wave observations with AIRS and IASI. Atmosp Meas Techn 7(12):4517–4537

Huba JD, Drob DP, Wu T-W, Makela JJ (2015) Modeling the ionospheric impact of tsunami-driven gravity waves with SAMI3: conjugate effects. Geophys Res Lett 42(14):5719–5726. https://doi.org/10.1002/2015GL064871

Hohensinn R, Aichinger-Rosenberger M, Wareyka-Glaner MF, Ravanelli M (2024) Natural hazard monitoring with global navigation satellite systems (GNSS). In: Space geodesy for environmental monitoring. Elsevier, pp 1–123

Igarashi K, Kainuma S, Nishimuta I, Okamoto S, Kuroiwa H, Tanaka T, Ogawa T (1994) Ionospheric and atmospheric disturbances around Japan caused by the eruption of mount Pinatubo on 15 June 1991. J Atmos Terr Phys 56(9):1227–1234. https://doi.org/10.1016/0021-9169(94)90060-4

Immel TJ, England SL, Harding BJ, Wu Y-J, Maute A, Cullens C, Englert CR, Mende SB, Heelis RA, Frey HU et al (2023) The ionospheric connection explorer-prime mission review. Space Sci Rev 219(5):41

Immel TJ, England S, Mende S, Heelis R, Englert C, Edelstein J, Frey H, Korpela E, Taylor E, Craig W et al (2018) The ionospheric connection explorer mission: mission goals and design. Space Sci Rev 214:1–36

Inchin PA, Guerrero JA, Snively JB, Kaneko Y (2022) Simulation of infrasonic acoustic wave imprints on airglow layers during the 2016 M7.8 Kaikoura earthquake. J Geophys Res Space Phys 127(3):2021–029529. https://doi.org/10.1029/2021JA029529

Inchin PA, Heale CJ, Snively JB, Zettergren MD (2020) The dynamics of nonlinear atmospheric acoustic-gravity waves generated by tsunamis over realistic bathymetry. J Geophys Res Space Phys 125(12):2020–028309. https://doi.org/10.1029/2020JA028309

Inchin PA, Heale CJ, Snively JB, Zettergren MD (2022) Numerical modeling of tsunami-generated acoustic-gravity waves in mesopause airglow. J Geophys Res Space Phys 127(8):2022–030301. https://doi.org/10.1029/2022JA030301

Inchin PA, Snively JB, Kaneko Y, Zettergren MD, Komjathy A (2021) Inferring the evolution of a large earthquake from its acoustic impacts on the ionosphere. AGU Adv 2(2):2020. https://doi.org/10.1029/2020AV000260

Inchin PA, Snively JB, Williamson A, Melgar D, Aguilar Guerrero J, Zettergren MD (2020) Mesopause airglow disturbances driven by nonlinear infrasonic acoustic waves generated by large earthquakes. J Geophys Res Space Phys 125(6):2019–027628. https://doi.org/10.1029/2019JA027628

Inchin PA, Snively JB, Zettergren MD, Komjathy A, Verkhoglyadova OP, Tulasi Ram S (2020) Modeling of ionospheric responses to atmospheric acoustic and gravity waves driven by the 2015 Nepal 7.8 Gorkha earthquake. J Geophys Res Space Phys 125(4):2019–027200. https://doi.org/10.1029/2019JA027200

Iyemori T, Nishioka M, Otsuka Y, Shinbori A (2022) A confirmation of vertical acoustic resonance and field-aligned current generation just after the 2022 Hunga Tonga Hunga Ha'apai volcanic eruption. Earth Planets Space 74(1):103

Jonah OF, Vergados P, Krishnamoorthy S, Komjathy A (2021) Investigating ionospheric perturbations following the 2020 Beirut explosion event. Radio Sci. https://doi.org/10.1029/2021RS007302

Jonah OF, Coster A, Zhang S, Goncharenko L, Erickson PJ, Paula E, Kherani EA (2018) TID observations and source analysis during the 2017 memorial day weekend geomagnetic storm over North America. J Geophys Res Space Phys 123(10):8749–8765

Kakinami Y, Kamogawa M, Tanioka Y, Watanabe S, Gusman AR, Liu J-Y, Watanabe Y, Mogi T (2012) Tsunamigenic ionospheric hole. Geophys Res Lett 39(13)

Kakinami Y, Kamogawa M, Watanabe S, Odaka M, Mogi T, Liu JY, Sun YY, Yamada T (2013) Ionospheric ripples excited by superimposed wave fronts associated with Rayleigh waves in the thermosphere. J Geophys Res Space Phys 118(2):905–911. https://doi.org/10.1002/jgra.50099

Kamogawa M, Kanaya T, Orihara Y, Toyoda A, Suzuki Y, Togo S, Liu J-Y (2015) Does an ionospheric hole appear after an inland earthquake? J Geophys Res Space Phys 120(11):9998–10005

Kamogawa M, Orihara Y, Tsurudome C, Tomida Y, Kanaya T, Ikeda D, Gusman AR, Kakinami Y, Liu J-Y, Toyoda A (2016) A possible space-based tsunami early warning system using observations of the tsunami ionospheric hole. Sci Rep 6(1):37989. https://doi.org/10.1038/srep37989

Kanamori H, Mori J, Harkrider DG (1994) Excitation of atmospheric oscillations by volcanic eruptions. J Geophys Res Solid Earth 99(B11):21947–21961. https://doi.org/10.1029/94JB01475

Kiryushkin VV, Afraimovich EL (2007) Determining the parameters of ionospheric perturbation caused by earthquakes using the quasi-optimum algorithm of spatiotemporal processing of TEC measurements. Earth Planets Space 59(4):267–278. https://doi.org/10.1186/BF03353104

Komjathy A, Yang YM, Meng X, Verkhoglyadova O, Mannucci AJ, Langley RB (2016) Review and perspectives: understanding natural-hazards-generated ionospheric perturbations using GPS measurements and coupled modeling. Radio Sci 51(7):951–961. https://doi.org/10.1002/2015RS005910

Kramer R, Wüst S, Schmidt C, Bittner M (2015) Gravity wave characteristics in the middle atmosphere during the CESAR campaign at Palma de Mallorca in 2011/2012: impact of extratropical cyclones and cold fronts. J Atmos Solar Terr Phys 128:8–23

Krassovsky V (1972) Infrasonic variation of OH emission in the upper atmosphere. Ann Geophys 28:739–746

Kuo CL, Lee LC, Huba JD (2014) An improved coupling model for the lithosphere-atmosphere-ionosphere system. J Geophys Res Space Phys 119:3189–3205. https://doi.org/10.1002/2013JA019392

Landerer FW, Flechtner FM, Save H, Webb FH, Bandikova T, Bertiger WI, Bettadpur SV, Byun SH, Dahle C, Dobslaw H et al (2020) Extending the global mass change data record: GRACE follow-on instrument and science data performance. Geophys Res Lett 47(12):2020–088306

Le Dû T, Simoneau P, Keckhut P, Hauchecorne A, Le Pichon A (2020) Investigation of infrasound signatures from microbaroms using oh airglow and ground-based microbarometers. Adv Space Res 65(3):902–908. https://doi.org/10.1016/j.asr.2019.11.026

Lee RF, Rolland LM, Mikesell TD (2018) Seismo-ionospheric observations, modeling, and backprojection of the 2016 Kaikōura earthquake. Bull Seismol Soc Am 108(3B):1794–1806. https://doi.org/10.1785/0120170299

Leonard RS, Barnes RA (1965) Observation of ionospheric disturbances following the Alaska earthquake. J Geophys Res (1896–1977) 70(5):1250–1253. https://doi.org/10.1029/JZ070i005p01250

Li R, Lei J, Kusche J, Dang T, Huang F, Luan X, Zhang S-R, Yan M, Yang Z, Liu F et al (2023) Large-scale disturbances in the upper thermosphere induced by the 2022 Tonga volcanic eruption. Geophys Res Lett 50(3):2022–102265

Lin JW (2022) Generalized two-dimensional principal component analysis and two artificial neural network models to detect traveling ionospheric disturbances. Nat Hazards 111(2):1245–1270. https://doi.org/10.1007/s11069-021-05093-x

Liu CH, Klostermeyer J, Yeh KC, Jones TB, Robinson T, Holt O, Leitinger R, Ogawa T, Sinno K, Kato S, Ogawa T, Bedard AJ (1980) Kersley L (1982) Global dynamic responses of the atmosphere to the eruption of Mount St. Helens on May 18. J Geophys Res Space Phys 87(A8):6281–6290. https://doi.org/10.1029/JA087iA08p06281

Liu JY, Tsai HF, Lin CH, Kamogawa M, Chen YI, Lin CH, Huang BS, Yu SB, Yeh YH (2010) Coseismic ionospheric disturbances triggered by the Chi-Chi earthquake. J Geophys Res Space Phys. https://doi.org/10.1029/2009JA014943

Liu J-YT, Shen X, Chang F-Y, Chen Y-I, Sun Y-Y, Chen C-H, Pulinets S, Hattori K, Ouzounov D, Tramutoli V, Parrot M, Chen W-S, Liu C-Y, Zhang F, Liu D, Zhang RX-M, Yan WQ (2024) Spatial analyses on pre-earthquake ionospheric anomalies and magnetic storms observed by China seismo-electromagnetic satellite in August 2018. Geosci Lett. https://doi.org/10.1186/s40562-024-00320-2

Liu J-Y, Lin C-Y, Chen Y-I, Wu T-R, Chung M-J, Liu T-C, Tsai Y-L, Chang LC, Chao C-K, Ouzounov D, Hattori K (2020) The source detection of 28 September 2018 Sulawesi tsunami by using ionospheric GNSS total electron content disturbance. Geosci Lett 7(1):11. https://doi.org/10.1186/s40562-020-00160-w

Liu J, Chen C, Chen Y, Yang W, Oyama K, Kuo K (2010) A statistical study of ionospheric earthquake precursors monitored by using equatorial ionization anomaly of GPS TEC in taiwan during 2001–2007. J Asian Earth Sci 39:76–80

Liu L, Morton YJ, Cheng P-H, Amores A, Wright CJ, Hoffmann L (2023) Concentric traveling ionospheric disturbances (CTIDs) triggered by the 2022 Tonga volcanic eruption. J Geophys Res Space Phys. https://doi.org/10.1029/2022JA030656

Liu X, Zhang Q, Shah M, Hong Z (2017) Atmospheric-ionospheric disturbances following the April 2015 Calbuco volcano from GPS and OMI observations. Adv Space Res 60(12):2836–2846. https://doi.org/10.1016/j.asr.2017.07.007

Lognonné P, Garcia R, Crespon F, Occhipinti G, Kherani E, Lambin J (2006) Seismic waves in the ionosphere. Europhys News 37:11–15. https://doi.org/10.1051/epn:2006401

Lognonné P, Artru J, Garcia R, Crespon F, Ducic V, Jeansou E, Occhipinti G, Helbert J, Moreaux G, Godet P-E (2006) Ground-based GPS imaging of ionospheric post-seismic signal. Planet Space Sci 54(5):528–540. https://doi.org/10.1016/j.pss.2005.10.021

Luhrmann F, Park J, Wong W-K, Corcoran F, Lewis C (2022) Detecting traveling ionospheric disturbances with LSTM based anomaly detection. In: Proceedings of the 35th international technical meeting of the satellite division of the institute of navigation (ION GNSS+ 2022), Denver, Colorado, pp 3002–3011. https://doi.org/10.33012/2022.18343

Lyons LR, Nishimura Y, Zhang S-R, Coster AJ, Bhatt A, Kendall E, Deng Y (2019) Identification of auroral zone activity driving large-scale traveling ionospheric disturbances. J Geophys Res Space Phys 124(1):700–714

Madonia P, Bonaccorso A, Bonforte A, Buonocunto C, Cannata A, Carleo L, Cesaroni C, Currenti G, De Gregorio S, Di Lieto B, Guerra M, Orazi M, Pasotti L, Peluso R, Pezzopane M, Restivo V, Romano P, Sciotto M, Spogli L (2023) Propagation of perturbations in the lower and upper atmosphere over the central mediterranean, driven by the 15 January 2022 Hunga Tonga-Hunga Ha'apai volcano explosion. Atmosphere 14(1):65. https://doi.org/10.3390/atmos14010065

Maletckii B, Astafyeva E (2022) Near-real-time analysis of the ionospheric response to the 15 January 2022 Hunga Tonga-Hunga Ha'apai volcanic eruption. J Geophys Res Space Phys 127(10):2022–030735. https://doi.org/10.1029/2022JA030735

Maletckii B, Astafyeva E (2024) Near-real-time identification of the source of ionospheric disturbances. J Geophys Res Space Phys 129(11):2024–032664. https://doi.org/10.1029/2024JA032664

Maletckii B, Astafyeva E, Sanchez SA, Kherani EA, Paula ER (2023) The 6 February 2023 Türkiye earthquake sequence as detected in the ionosphere. J Geophys Res Space Phys 128(9):2023–031663. https://doi.org/10.1029/2023JA031663

Maletckii B, Astafyeva E (2021) Determining spatio-temporal characteristics of coseismic travelling ionospheric disturbances (CTID) in near real-time. Sci Rep. https://doi.org/10.1038/s41598-021-99906-5

Manta F, Occhipinti G, Feng L, Hill EM (2020) Rapid identification of tsunamigenic earthquakes using GNSS ionospheric sounding. Sci Rep 10(1):11054. https://doi.org/10.1038/s41598-020-68097-w

Manta F, Occhipinti G, Hill EM, Perttu A, Assink J, Taisne B (2021) Correlation between GNSS-TEC and eruption magnitude supports the use of ionospheric sensing to complement volcanic hazard assessment. J Geophys Res Solid Earth. https://doi.org/10.1029/2020JB020726

Martinis C, Baumgardner J, Wroten J, Mendillo M (2011) All-sky imaging observations of conjugate medium-scale traveling ionospheric disturbances in the american sector. J Geophys Res (Space Phys) 116(A5):05326. https://doi.org/10.1029/2010JA016264

Martire L, Krishnamoorthy S, Vergados P, Romans LJ, Szilágyi B, Meng X, Anderson JL, Komjáthy A, Bar-Sever YE (2022) The GUARDIAN system-a GNSS upper atmospheric real-time disaster information and alert network. GPS Solut 27(1):32. https://doi.org/10.1007/s10291-022-01365-6

Maruyama T, Tsugawa T, Kato H, Ishii M, Nishioka M (2012) Rayleigh wave signature in ionograms induced by strong earthquakes. J Geophys Res Space Phys. https://doi.org/10.1029/2012JA017952

Maruyama T, Yusupov K, Akchurin A (2016) Ionosonde tracking of infrasound wavefronts in the thermosphere launched by seismic waves after the 2010 M8.8 Chile earthquake. J Geophys Res Space Phys 121(3):2683–2692. https://doi.org/10.1002/2015JA022260

Meinel AB (1950) OH emission bands in the spectrum of the night sky. Astrophys J 111:555

Najita K (1976) Engineering feasibility study of an ionospheric technique to improve tsunami warning systems. University of Hawaii, Hawaii, USA

Nakamura T, Higashikawa A, Tsuda T, Matsushita Y (1999) Seasonal variations of gravity wave structures in OH airglow with a CCD imager at shigaraki. Earth Planets Space 51:897–906

Nakashima Y, Heki K, Takeo A, Cahyadi MN, Aditiya A, Yoshizawa K (2016) Atmospheric resonant oscillations by the 2014 eruption of the Kelud volcano, Indonesia, observed with the ionospheric total electron contents and seismic signals. Earth Planet Sci Lett 434:112–116. https://doi.org/10.1016/j.epsl.2015.11.029

Nappo CJ (2012) An introduction to atmospheric gravity waves. Academic press, Amsterdam, Netherlands

Nemec F, Santolik O, Parrot M, Berthelier J (2008) Spacecraft observations of electromagnetic perturbations connected with seismic activity. Geophys Res Lett. https://doi.org/10.1029/2007GL032517

Meng X, Vergados P, Komjathy A, Verkhoglyadova O (2019) Upper atmospheric responses to surface disturbances: an observational perspective. Radio Sci 54(11):1076–1098. https://doi.org/10.1029/2019RS006858

Occhipinti G, Aden-Antoniow F, Bablet A, Molinie J-P, Farges T (2018) Surface waves magnitude estimation from ionospheric signature of Rayleigh waves measured by doppler sounder and OTH radar. Sci Rep 8(1):1555. https://doi.org/10.1038/s41598-018-19305-1

Olsen N, Friis-Christensen E, Floberghagen R, Alken P, Beggan CD, Chulliat A, Doornbos E, Encarnação JT, Hamilton B, Hulot G et al (2013) The Swarm satellite constellation application and research facility (scarf) and swarm data products. Earth Planets Space 65:1189–1200

Pichler H (1997) Dynamik der Atmosphäre. Spektrum Akademischer Verlag GmbH, Mannheim, Germany

Pilger C, Schmidt C, Bittner M (2013) Statistical analysis of infrasound signatures in airglow observations: Indications for acoustic resonance. J Atmosp Solar-Terrestr Phys 93:70–79. https://doi.org/10.1016/j.jastp.2012.11.011

Pilger C, Schmidt C, Streicher F, Wüst S, Bittner M (2013) Airglow observations of orographic, volcanic and meteorological infrasound signatures. J Atmosp Solar-Terrest Phys 104:55–66. https://doi.org/10.1016/j.jastp.2013.08.008

Pulinets S, Davidenko D (2014) Ionospheric precursors of earthquakes and global electric circuit. Adv Space Res 53:709–723. https://doi.org/10.1016/j.asr.2013.12.035

Rakoto V, Lognonné P, Rolland L, Coïsson P (2018) Tsunami wave height estimation from GPS-derived ionospheric data. J Geophys Res Space Phys 123(5):4329–4348. https://doi.org/10.1002/2017JA024654

Rauthe M, Gerding M, Lübken F-J (2008) Seasonal changes in gravity wave activity measured by lidars at mid-latitudes. Atmos Chem Phys 8(22):6775–6787

Ravanelli M, Astafyeva E, Munaibari E, Rolland L, Mikesell TD (2023) Ocean-ionosphere disturbances due to the 15 January 2022 Hunga-Tonga Hunga-Ha'apai eruption. Geophys Res Lett 50(10):2022–101465. https://doi.org/10.1029/2022GL101465

Ravanelli M, Constantinou V, Liu H, Bortnik J (2024) Exploring ai progress in GNSS remote sensing: a deep learning based framework for real-time detection of earthquake and tsunami induced ionospheric perturbations. Radio Sci 59(9):2024–008016. https://doi.org/10.1029/2024RS008016

Riabova SA, Shalimov SL (2024) Response of the lower and upper ionosphere after the eruption of Shiveluch volcano on April 10, 2023. Geomag Aeron 64(1):94–101. https://doi.org/10.1134/S001679322360087X

Rolland LM, Lognonné P, Munekane H (2011) Detection and modeling of Rayleigh wave induced patterns in the ionosphere. J Geophys Res Space Phys. https://doi.org/10.1029/2010JA016060

Rolland LM, Vergnolle M, Nocquet JM, Sladen A, Dessa JX, Tavakoli F, Nankali HR, Cappa F (2013) Discriminating the tectonic and non-tectonic contributions in the ionospheric signature of the 2011, Mw7.1, dip-slip Van earthquake, Eastern Turkey. Geophys Res Lett 40(11):2518–2522. https://doi.org/10.1002/grl.50544

Saito A, Tsugawa T, Otsuka Y, Nishioka M, Iyemori T, Matsumura M, Saito S, Chen C, Goi Y, Choosakul N (2011) Acoustic resonance and plasma depletion detected by GPS total electron content observation after the 2011 off the pacific coast of Tohoku earthquake. Earth Planets Space 63:863–867

Savastano G, Komjathy A, Verkhoglyadova O, Mazzoni A, Crespi M, Wei Y, Mannucci AJ (2017) Real-time detection of tsunami ionospheric disturbances with a stand-alone GNSS receiver: A preliminary feasibility demonstration. Sci Rep. https://doi.org/10.1038/srep46607

Savastano G, Ravanelli M (2019) Real-time monitoring of ionospheric irregularities and TEC perturbations. In: Demyanov V, Becedas J (eds) Satellites missions and technologies for geosciences. IntechOpen, London. https://doi.org/10.5772/intechopen.90036

Schmit TJ, Griffith P, Gunshor MM, Daniels JM, Goodman SJ, Lebair WJ (2017) A closer look at the ABI on the GOES-R series. Bull Am Meteor Soc 98(4):681–698

Sedlak R, Hannawald P, Schmidt C, Wüst S, Bittner M (2016) High-resolution observations of small-scale gravity waves and turbulence features in the oh airglow layer. Atmosp Meas Techn 9(12):5955–5963. https://doi.org/10.5194/amt-9-5955-2016

Shepherd GG, Cho Y-M, Liu G, Shepherd MG, Roble RG (2006) Airglow variability in the context of the global mesospheric circulation. J Atmosp Solar-Terrestr Phys 68(17):2000–2011. https://doi.org/10.1016/j.jastp.2006.06.006

Shinagawa H, Tsugawa T, Matsumura M, Iyemori T, Saito A, Maruyama T, Jin H, Nishioka M, Otsuka Y (2013) Two-dimensional simulation of ionospheric variations in the vicinity of the epicenter of the Tohoku-Oki earthquake on 11 March 2011. Geophys Res Lett 40(19):5009–5013

Shinbori A, Otsuka Y, Sori T, Nishioka M, Perwitasari S, Tsuda T, Nishitani N (2022) Electromagnetic conjugacy of ionospheric disturbances after the 2022 Hunga Tonga-Hunga Ha'apai volcanic eruption as seen in GNSS-TEC and SuperDARN hokkaido pair of radars observations. Earth Planets Space 74(1):106

Shults K, Astafyeva E, Adourian S (2016) Ionospheric detection and localization of volcano eruptions on the example of the April 2015 Calbuco events. J Geophys Res Space Phys 121(10):10303–10315. https://doi.org/10.1002/2016JA023382

Snively JB (2013) Mesospheric hydroxyl airglow signatures of acoustic and gravity waves generated by transient tropospheric forcing. Geophys Res Lett 40(17):4533–4537. https://doi.org/10.1002/grl.50886

Sridharan R, Modi N, Raju DP, Narayanan R, Pant TK, Taori A, Chakrabarty D (1998) A multiwavelength daytime photometer-a new tool for the investigation of atmospheric processes. Meas Sci Technol 9(4):585. https://doi.org/10.1088/0957-0233/9/4/005

Sun Y-Y, Chen C-H, Lin C-Y (2022) Detection of vertical changes in the ionospheric electron density structures by the radio occultation technique onboard the FORMOSAT-7/COSMIC-2 mission over the eruption of the Tonga underwater volcano on 15 January 2022. Remote Sens 14(17):4266

Sun Y-Y, Liu J-Y, Lin C-Y, Tsai H-F, Chang LC, Chen C-Y, Chen C-H (2016) Ionospheric F2 region perturbed by the 25 April 2015 Nepal earthquake. J Geophys Res Space Phys 121(6):5778–5784

Suzuki S, Shiokawa K, Otsuka Y, Ogawa T, Wilkinson P (2004) Statistical characteristics of gravity waves observed by an all-sky imager at Darwin, Australia. J Geophys Res Atmosp. https://doi.org/10.1029/2003JD004336

Swenson GR, Gardner CS (1998) Analytical models for the responses of the mesospheric OH* and Na layers to atmospheric gravity waves. J Geophys Res Atmosp 103(D6):6271–6294

Tapley BD, Bettadpur S, Ries JC, Thompson PF, Watkins MM (2004) GRACE measurements of mass variability in the earth system. Science 305(5683):503–505

Themens DR, Watson C, Žagar N, Vasylkevych S, Elvidge S, McCaffrey A, Prikryl P, Reid B, Wood A, Jayachandran PT (2022) Global propagation of ionospheric disturbances associated with the 2022 Tonga volcanic eruption. Geophys Res Lett 49(7):2022–098158. https://doi.org/10.1029/2022GL098158

Tsai H-F, Liu J-Y, Lin C-H, Chen C-H (2011) Tracking the epicenter and the tsunami origin with GPS ionosphere observation. Earth Planets Space 63(7):859–862. https://doi.org/10.5047/eps.2011.06.024

Tsugawa T, Saito A, Otsuka Y, Nishioka M, Maruyama T, Kato H, Nagatsuma T, Murata K (2011) Ionospheric disturbances detected by GPS total electron content observation after the 2011 off the Pacific coast of Tohoku earthquake. Earth Planets Space 63:875–879

Tyska J, Deng Y, Zhang S, Lin CY (2024) Ionospheric disturbances generated by the 2015 Calbuco eruption: comparison of GITM-R simulations and GNSS observations. Space Weather 22(2):2023–003502. https://doi.org/10.1029/2023SW003502

Vadas SL, Becker E, Figueiredo C, Bossert K, Harding BJ, Gasque LC (2023) Primary and secondary gravity waves and large-scale wind changes generated by the Tonga volcanic eruption on 15 January 2022: modeling and comparison with ICON-MIGHTI winds. J Geophys Res Space Phys 128(2):2022–031138

Vadas SL, Fritts DC (2005) Thermospheric responses to gravity waves: Influences of increasing viscosity and thermal diffusivity. J Geophys Res Atmosp 110(D15)

Verhulst TGW, Altadill D, Barta V, Belehaki A, Burešová D, Cesaroni C, Galkin I, Guerra M, Ippolito A, Herekakis T, Kouba D, Mielich J, Segarra A, Spogli L, Tsagouri I (2022) Multi-instrument detection in Europe of ionospheric disturbances caused by the 15 January 2022 eruption of the Hunga volcano. J Space Weather Space Clim 12:35. https://doi.org/10.1051/swsc/2022032

von Savigny C (2015) Variability of OH(3–1) emission altitude from 2003 to 2011: Long-term stability and universality of the emission rate-altitude relationship. J Atmosp Solar-Terrest Phys 127:120–128. https://doi.org/10.1016/j.jastp.2015.02.001

Wachter P, Schmidt C, Wüst S, Bittner M (2015) Spatial gravity wave characteristics obtained from multiple OH(3–1) airglow temperature time series. J Atmosp Solar-Terrestr Phys 135:192–201. https://doi.org/10.1016/j.jastp.2015.11.008

Wright CJ, Hindley NP, Alexander MJ, Barlow M, Hoffmann L, Mitchell CN, Prata F, Bouillon M, Carstens J, Clerbaux C, Osprey SM, Powell N, Randall CE, Yue J (2022) Surface-to-space atmospheric waves from Hunga Tonga-Hunga Ha'apai eruption. Nature 609(7928):741–746

Wüst S, Wendt V, Schmidt C, Lichtenstern S, Bittner M, Yee J-H, Mlynczak MG, Russell JM (2016) Derivation of gravity wave potential energy density from NDMC measurements. J Atmosp Solar-Terrestr Phys 138:32–46. https://doi.org/10.1016/j.jastp.2015.12.003

Wüst S, Schmidt C, Bittner M, Silber I, Price C, Yee J-H, Mlynczak MG, Russell JM III (2017a) First ground-based observations of mesopause temperatures above the Eastern-Mediterranean Part II: OH*-climatology and gravity wave activity. J Atmosp Solar-Terrest Phys 155:104–111. https://doi.org/10.1016/j.jastp.2017.01.003

Wüst S, Bittner M, Yee J-H, Mlynczak MG, Russell JM (2017b) Variability of the Brunt-Väisälä frequency at the OH* layer height. Atmosp Meas Techn 10(12):4895–4903. https://doi.org/10.5194/amt-10-4895-2017

Wüst S, Offenwanger T, Schmidt C, Bittner M, Jacobi C, Stober G, Yee J-H, Mlynczak MG, Russell JM (2018) Derivation of gravity wave intrinsic parameters and vertical wavelength using a single scanning OH(3–1) airglow spectrometer. Atmosp Meas Techn 11(5):2937–2947. https://doi.org/10.5194/amt-11-2937-2018

Wüst S, Bittner M, Yee J-H, Mlynczak MG, Russell JM (2020) Variability of the Brunt-Väisälä frequency at the OH-airglow layer height at low and midlatitudes. Atmosp Meas Techn 13(11):6067–6093. https://doi.org/10.5194/amt-13-6067-2020

Wüst S, Bittner M, Espy PJ, French WJR, Mulligan FJ (2023) Hydroxyl airglow observations for investigating atmospheric dynamics: results and challenges. Atmos Chem Phys 23(2):1599–1618. https://doi.org/10.5194/acp-23-1599-2023

Wüst S, Küchelbacher L, Trinkl F, Bittner M (2025) Gravity waves above the northern Atlantic and Europe during streamer events using Aeolus. Atmosp Meas Techn. https://doi.org/10.5194/amt-18-1591-2025

Yamazaki Y, Soares G, Matzka J (2022) Geomagnetic detection of the atmospheric acoustic resonance at 3.8 mHz during the Hunga Tonga eruption event on 15 January 2022. J Geophys Res Space Phys 127(7):2022–030540

Yang H, Monte-Moreno E, Hernández-Pajares M (2017) Multi-TID detection and characterization in a dense Global Navigation Satellite System receiver network. J Geophys Res Space Phys 122(9):9554–9575. https://doi.org/10.1002/2017JA023988

Yang H, Moreno EM, Hernández-Pajares M (2019) ADDTID: an alternative tool for studying earthquake/tsunami signatures in the ionosphere. Case of the 2011 Tohoku earthquake. Remote Sens. https://doi.org/10.3390/rs11161894

Yeh KC, Liu CH (1974) Acoustic-gravity waves in the upper atmosphere. Rev Geophys 12(2):193–216

Zettergren MD, Snively JB (2015) Ionospheric response to infrasonic-acoustic waves generated by natural hazard events. J Geophys Res Space Phys 120(9):8002–8024. https://doi.org/10.1002/2015JA021116

Zettergren M, Snively J (2019) Latitude and longitude dependence of ionospheric TEC and magnetic perturbations from infrasonic-acoustic waves generated by strong seismic events. Geophys Res Lett 46(3):1132–1140

Zettergren M, Snively J, Komjathy A, Verkhoglyadova O (2017) Nonlinear ionospheric responses to large-amplitude infrasonic-acoustic waves generated by undersea earthquakes. J Geophys Res Space Phys 122(2):2272–2291

Authors and Affiliations

Sabine Wüst[1] · Marco Guerra[2,3] · Jaroslav Chum[4] · L. Claire Gasque[5]

✉ Sabine Wüst
sabine.wuest@dlr.de

Marco Guerra
marco.guerra@ingv.it

Jaroslav Chum
jachu@ufa.cas.cz

L. Claire Gasque
lcgasque@berkeley.edu

[1] Erdbeobachtungszentrum (EOC), Deutsches Zentrum für Luft- und Raumfahrt e.V. (DLR), 82234 Wessling, Germany

[2] Dipartimento di ingegneria Informatica Automatica e Gestionale (DIAG), Sapienza Università di Roma, 00185 Rome, Italy

[3] Sezione Roma 2, Istituto Nazionale di Geofisica e Vulcanologia (INGV), 00143 Rome, Italy

[4] Institute of Atmospheric Physics (IAP), Czech Academy of Sciences (CAS), 14100 Prague 4, Czech Republic

[5] Space Sciences Laboratory, University of California Berkeley, 7 Gauss Way, Berkeley, CA 94720, USA